Available online at www.sciencedirect.com
SCIENCE DIRECT
Lithos 89 (2006) 174–201
LITHOS
www.elsevier.com/locate/lithos

Dating of subduction and differential exhumation of UHP rocks from the Central Dabie Complex (E-China): Constraints from microfabrics, Rb–Sr and U–Pb isotope systems

Nicole Wawrzenitz [a,b,*], Rolf L. Romer [a], Roland Oberhänsli [b], Shuwen Dong [c]

[a] GeoForschungsZentrum Potsdam, Telegrafenberg, D-14473 Potsdam, Germany
[b] Institut für Geowissenschaften, Universität Potsdam, D-14476 Potsdam, Germany
[c] Institute of Geomechanics, Chinese Academy of Geological Sciences, Beijing 100081, China

Received 14 June 2005; accepted 12 December 2005
Available online 24 January 2006

Abstract

The correlation of deformation fabrics and metamorphic reactions with geochronologic data of UHP metamorphic rocks demonstrate that the multistage subduction and exhumation history of the Central Dabie Complex requires rapid subduction and rapid initial exhumation. Moreover, these data show that volume diffusion is not the major resetting mechanism of radiogenic isotope systems. Thus, our age data do not simply reflect a thermal/cooling history. In the investigated section, the maximum age for UHP is given by the 244 ± 3 Ma (2σ) U–Pb age of a pre-UHP titanite phenocryst that survived UHP metamorphism and subsequent tectonometamorphic events. A minimum age for UHP is set by the 238 ± 1 Ma (2σ) ^{238}U–^{206}Pb mineral isochron age of titanite and cogenetic epidote. These minerals formed from local partial melts during ascent and their age suggests fast exhumation and emplacement in the middle crust. In the period of ca. 238–218 Ma, the UHP terrain records HT metamorphism, local partial melting, and extensive pervasive strain below the eclogite (jd+grt) stability field. Exhumation was polyphase with a first phase of fast exhumation, succeeded by episodes of HT metamorphism and concomitant deformation at deep/mid crustal level between 238 and 218 Ma. Slow exhumation related to the final emplacement of tectonic units along greenschist facies shear zones did not cease before ca. 209–204 Ma. The resetting and homogenization of radiogenic isotope systems were aided by dissolution precipitation creep, which was the dominant deformation mechanism in quartz–feldspar rocks, in combination with fluid influx.

Keywords: UHP metamorphism; Exhumation; Deformation; U–Pb Rb–Sr Sm–Nd isotope dating; Titanite; Dabie Shan

1. Introduction and scope of work

During UHP metamorphism, crustal rocks are brought to extreme conditions. Large density contrasts to the surrounding mantle material result in large buoyancy forces and rapid exhumation of UHP terranes, which facilitate the conservation of UHP mineral assemblages and microfabrics from several stages of the subduction and exhumation history. Probably, partial melting of subducted material plays an important role for its mechanical behaviour during ascent, in accordance with very rapid initial exhumation pulses (Wallis et al., 2005).

For the precise dating of distinct metamorphic stages of the *PTt*d path of a UHP terrain, it is fundamental to understand how changing deformation mechanisms and

* Corresponding author. GeoForschungsZentrum Potsdam, Telegrafenberg, D-14473 Potsdam, Germany. Tel.: +49 331 9678370.
E-mail address: nicole_wawr@gmx.de (N. Wawrzenitz).

0024-4937/$ - see front matter © 2005 Elsevier B.V. All rights reserved.
doi:10.1016/j.lithos.2005.12.001

metamorphic reactions over such a large *PT* interval, as well as fluid infiltration at successive stages during subduction and ascent, affect the geochronological record of UHP rocks. To model mass transfer along convergent plate boundaries, it is necessary to know the duration of subduction, the time of exposure to the UHP conditions, the exhumation rates, and the shape of the *PT*-paths of UHP terrains, especially whether exhumation of UHP rocks was the result of one or several stages.

The aim of this paper is to combine geochronological and microtectonic investigations to constrain the subduction and exhumation history of polymetamorphic UHP rocks from the Qinling–Dabie–Sulu metamorphic belt (Eastern China). We selected the Central Dabie Complex as study area, because (i) UHP relics are abundantly preserved and peak *P–T* conditions have been established by numerous petrological investigations (e.g., Okay et al., 1989; Wang and Liou, 1991; Okay, 1993; Carswell et al., 2000; Xiao et al., 2000; Schmid et al., 2000, 2003), (ii) the Central Dabie Complex preserves relics of different prograde and retrograde stages of the metamorphic and tectonic history. Such relics are predominantly preserved in high viscosity domains. During decompression and exhumation large strain within the Central Dabie Complex transposed the former sedimentary layering at low angle to the foliation. This implies high translation magnitudes.

In this paper, we present titanite U–Pb ages and white mica Rb–Sr ages from microstructurally different domains from the Central Dabie Complex. Titanite had grown during different prograde and retrograde stages of the *PTt*d paths. The microfabrics of the titanite bearing rocks reflect strain-induced diffusion-controlled processes such as dynamic recrystallization, recovery, and dissolution precipitation creep (diffusion creep, e.g., Passchier and Trouw, 1996), which enhance cation mobility on the grain scale and, thus, facilitate the homogenization of isotope systems. In contrast, material transport by dislocation creep would be restricted to the grain scale. Minerals from such domains could preserve an older U–Pb system.

Provided their U–Pb system remained closed, dating of titanite and cogenetic minerals may delineate successive metamorphic and deformational episodes (cf. Heaman and Parrish, 1991; Getty and Gromet, 1992; Freeman et al., 1997; Wawrzenitz and Krohe, 1998; Essex and Gromet, 2000; Romer, 2001). Hence, combined microtectonic, petrological, and geochronological studies of these rocks set constraints on the time interval between subduction to mantle depths and emplacement in the upper crust, as well as on the duration of UHP conditions and exhumation processes. Moreover, they potentially reveal the effect of deformation mechanisms and strain rate on radiogenic isotope systems (Krohe and Wawrzenitz, 2000).

2. Geological setting

The Qinling–Dabie–Sulu metamorphic belt (Eastern China) is the result of Triassic subduction and collision between the Yangtze craton (South China block) in the south and the Sino-Korean craton (North China block) in the north (Mattauer et al., 1985). The Dabie metamorphic belt consists of tectonic slivers characterized by a wide range of *P–T* conditions (Fig. 1). In the north, the low grade Foziling and Luzhenguan Complexes, also summarized as Beihuaiyang low-grade metamorphic zone, are interpreted by Zheng et al. (2005) as a passive-margin accretionary wedge deformed during continent subduction. Hacker et al. (2000) interpreted these complexes as a part of the overriding Sino-Korean craton. They are separated from the Yangtze UHP and HP units (Yangtze craton) to the south by the Xiaotian–Mozitan fault (being a normal detachment zone, e.g., Faure et al., 1999, 2003). These Yangtze units include: (i) the North Dabie Complex (formerly termed Northern Orthogneiss Unit), characterized by amphibolite facies gneisses, that locally contain UHP relics, such as microdiamonds in eclogite (Xu et al., 2003), as well as granulitic relics (Wang et al., 1998; Faure et al., 2003; Bryant et al., 2004), (ii) the Central Dabie Complex, in the literature commonly also termed Dabie ultrahigh-pressure (UHP; coesite–eclogite bearing) Complex, (iii) the South Dabie Complex, containing amphibolitized HP rocks, possibly also with UHP relics (Li et al., 2004), (iv) the Susong Blueschist Complex, and (v) the Yangtze fold-and-thrust belt. We use the neutral subdivision North, Central, and South Dabie, because UHP occurrences have been found in each unit (see below) and, therefore, the subdivision based on metamorphic grade and tectonic position has become ambiguous.

In the Central Dabie Complex, the occurrence of microdiamond constrains minimum *P* of ca. 30 kbar (Xu et al., 1992, 2003). Phase petrology in the UHP rocks indicates *PT* conditions of 42 kbar at 750 °C (Schmid et al., 2003), which implies exhumation from more than ca. 120 km depth. In the North Dabie Complex, minimum pressures attained in eclogitic lenses also allowed coesite and microdiamond formation (e.g., Xu et al., 2003; Xie et al., 2004). Early Cretaceous granitoids (ca. 130 Ma, U–Pb zircon data, Xue et

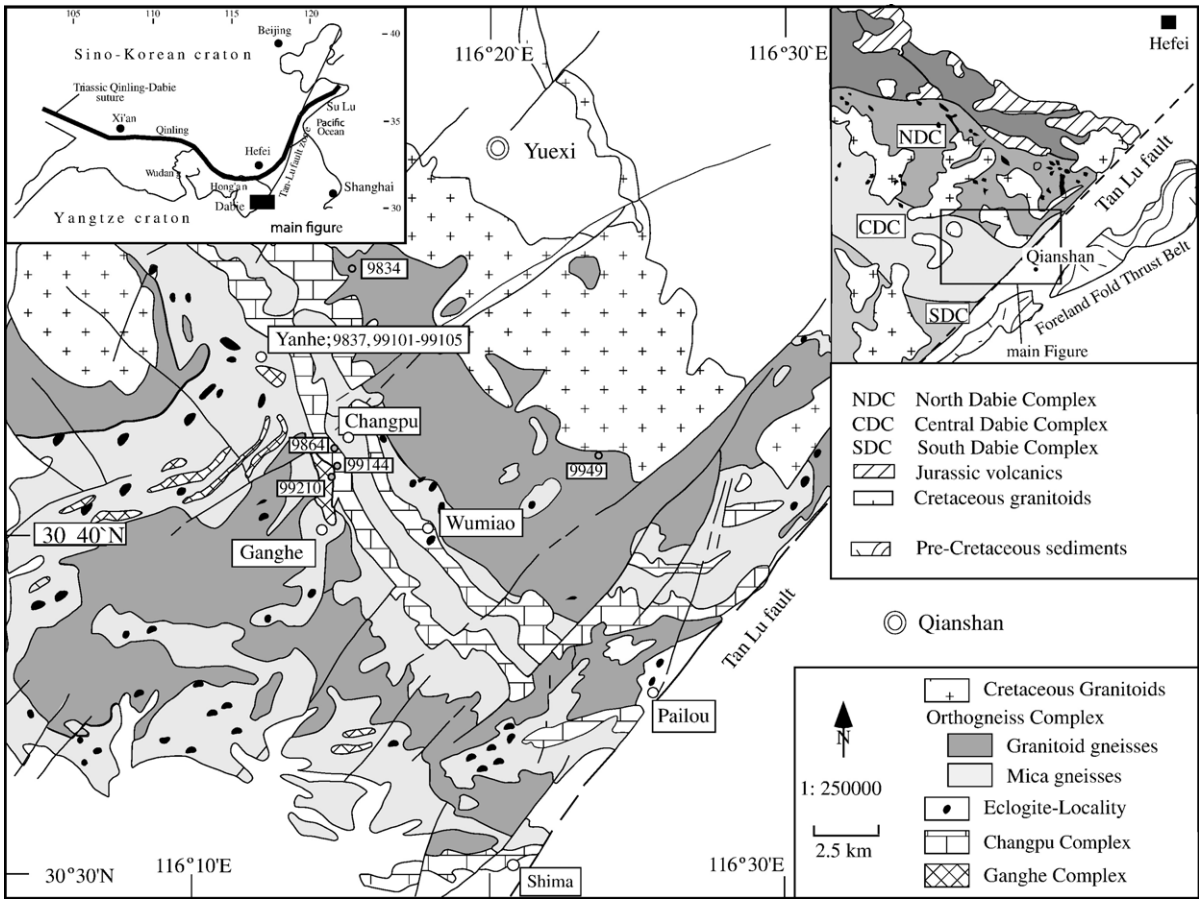

Fig. 1. Geological map showing the location of the study area in the Dabie Shan. Sample locations are indicated. Modified from Schmid (2001), based on unpublished mapping (1 : 250.000) of the Anhui Institute of Regional Geological Survey (AIRGS).

al., 1997; Hacker et al., 1998; Ratschbacher et al., 2000; Chen et al., 2002; Zhang et al., 2002a) intruded all these units, including supracrustal sediments and high grade migmatites. Contemporaneously, mafic to ultramafic igneous rocks were interpreted to have been generated by partial melting of metasomatized mantle (Jahn et al., 1999) or remelting of subducted lithosphere (Zhao et al., 2005), respectively.

Lithological successions composing the Central Dabie Complex represent reprocessed pre-Triassic basement rocks (Rowley et al., 1997; Maruyama et al., 1998) consisting of a Precambrian basement and its cover complexes. Basement lithologies include orthogenic gneisses, metabasites, and local ultramafic assemblages, in the following described as Orthogneiss Complex. The cover complexes (Changpu and Ganghe; Schmid, 2001; Oberhänsli et al., 2002; Schmid et al., 2003) are mainly composed of paragenic gneisses, calcsilicate rocks, metasediments, meta-volcanics, and meta-intrusives (Fig. 2).

Mineral relics of UHP metamorphism occur within the Orthogneiss Complex and the cover complexes, mostly in mafic eclogites and calcsilicate rocks. The Ganghe and the Changpu Cover Complex record slightly lower UHP peak conditions (37 kb/680 °C vs 42 kb/750 °C; Schmid, 2001).

All lithological units experienced ultra-high and/or high/medium-*P* metamorphism. During exhumation, these rocks were overprinted at high to medium pressure and slightly higher temperatures. Several phases of extensive strain under UHP metamorphism and during decompression/exhumation transposed the compositional layering and created a pervasive foliation. The various lithologies responded heterogeneously to differential stresses. For instance, the Ganghe Cover Complex contains relics of the prograde *PT*-path in low strain domains (Oberhänsli et al., 2002).

Large scale tectonic reconstructions based on combinations of petrologic, stable and radiogenic isotope

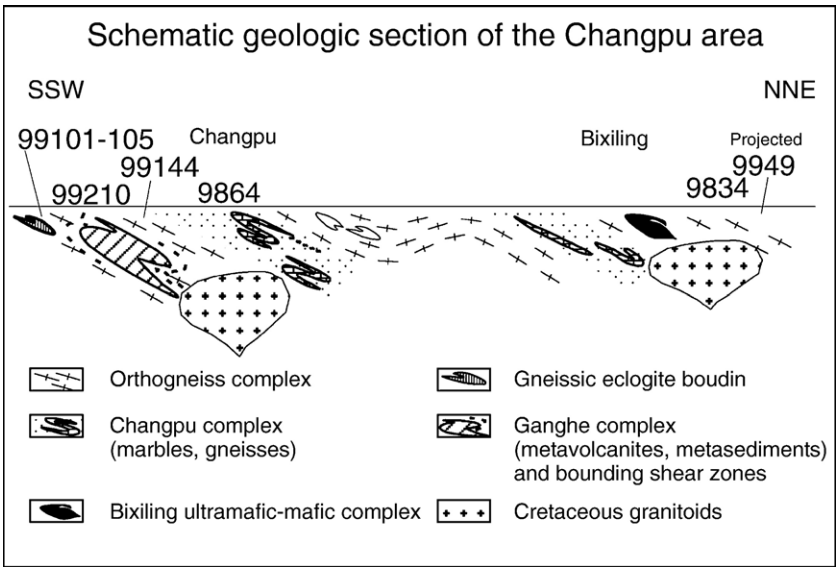

Fig. 2. Schematic section of the Central Dabie Complex indicating the location of the samples.

data, as well as fluid inclusion studies, were made by Jahn (1998), Zheng et al. (1998, 2003), Xiao et al. (2000), Schmid (2001), Fu et al. (2001), and based on regional thermal modelling and fission-track data by Webb et al. (1999), Ratschbacher et al. (2000), and Grimmer et al. (2002).

U–Pb zircon and monazite ages (236 ± 3, 223 ± 4, 209 ± 4 Ma; e.g., Ayers et al., 2002) and Sm–Nd mineral dating (226 ± 4 Ma) revealed that UHP metamorphism occurred about 240–225 Ma ago (see also Ames et al., 1993; Rowley et al., 1997; Chavagnac and Jahn, 1996; Hacker et al., 1998, 2000; Li et al., 2000, 2004). Protolith ages of these polymetamorphic rocks dominantly fall in the range of 700 to 800 Ma (e.g. Rowley et al., 1997; Hacker et al., 1998, 2000). Zircon cores, however, indicate ages up to 1.8 Ga (e.g., Maruyama et al., 1998).

Rb–Sr data from phengitic white mica and Ar–Ar mineral data from the UHP and HP units ranging between 225 and 210 Ma (Webb et al., 1999; Li et al., 2000, 2004) suggest various exhumation increments. Ar–Ar data from detrital phengitic mica in Mid-Jurassic foreland sediments to the south of the Dabie metamorphic belt yield ages as old as 240 ± 5 Ma (e.g., Grimmer et al., 2002).

Wang et al. (1998) consider the UHP and HP units an extensional allochthon that is separated by a Cretaceous extensional detachment system from the underlying North Dabie Complex. In contrast, Zhang et al. (2002a), Faure et al. (2003), and Bryant et al. (2004) interpret this boundary as a thrust belt that emplaced the UHP unit upon the gneisses of the North Dabie Complex. In the paper of Zhang et al. (2002a), structural considerations are used to suggest the undeformed Cretaceous intrusives, distributed throughout the Dabie metamorphic belt, to be genetically related to migmatites and orthogneisses of the North Dabie Complex. These rocks show similar retarded Pb isotopic compositions and Sr–Nd isotopic compositions as Cretaceous rocks intruding the UHP and HP units (Franz et al., 2001; Zhang et al., 2002a). In the North Dabie Complex, orthogneisses and migmatites contain boudins of UHP ultramafic rocks (garnet pyroxenites) that locally show Sm–Nd garnet, rutile, whole rock, clinopyroxene isochron ages of 219 ± 11 and 229 ± 13 Ma, indicating that parts of this unit also underwent Triassic UHP metamorphism (Xie et al., 2004) and that migmatization post-dates HP–UHP metamorphism (Faure et al., 2003). Eclogite xenoliths in Cretaceous granitoids (Faure et al., 2003) and microdiamonds (Xu et al., 2003, 2004) in this area are further indication of Triassic UHP metamorphism. Evidence for UHP metamorphism in the North Dabie Complex has also been documented by a petrological study of eclogite (Tsai and Liou, 2000).

3. Analyzed metamorphic rock samples

Quartz–feldspar and most calcsilicate rocks from the Central Dabie Complex are overprinted by intense strain under amphibolite facies conditions at temperatures above 600 °C (Liou et al., 1997). We analyzed mineral phases from samples containing microlithons (e.g., Bard, 1986) shielded from deformation during

decompression, and, thus, provide information on the prograde *PT*-path (sample 9864; GPS coordinates of sample locations are given in Appendix B). We also analyzed mineral phases from surrounding strained domains (samples 9949, 9834, 99101, 99104, and 99144), which are intensively deformed. Geochronological data from these mineral phases are expected to preserve the record of successive retrogressive stages: Our data show that such domains are characterized by pervasive recrystallization driven by dissolution precipitation creep at high temperatures. This was associated with fluid access and decomposition of essentially all UHP minerals. Locally, partial melting and crystallization from melts (sample 9949) in the stability field of plagioclase (MP) preceded dissolution precipitation creep. The combination of these processes facilitates resetting of radiogenic isotope systems (see discussion below). There is no deformation record for the exhumation path between UHP and medium pressure conditions. The access of water in advanced stages of the ascent history, however, favoured deformation (Mancktelow and Pennacchioni, 2004). During continued ascent, localization of strain into mylonites (e.g., sample 99210) is associated with increasing viscosity contrasts and formation of heterogeneously composed boudins at different scales.

3.1. Prograde titanite and pervasive strain during retrogressive metamorphism (calcsilicates, Changpu area; 9864)

3.1.1. Titanite generations

Calcsilicate rocks and marbles from the Changpu area locally preserve UHP peak pressure conditions (Fig. 3a). These rocks contain several generations of titanite (in contrast to the quartzofeldspathic rocks) that grew during the progressive and retrograde metamorphic evolution.

The oldest pre-deformational generation of titanite is only preserved in calcsilicate rocks. This titanite forms megacrysts and is older than the foliation. Due to the large viscosity contrast between titanite and carbonate (calcite or aragonite), it was not subjected to deformation. Sporadic rutile inclusions, as well as Al and F contents, suggest titanite formation at medium pressure. The titanite megacryst shows a homogeneous Al_2O_3 content with a slight Al_2O_3 increase towards the margin, which reflects pressure increase (Fig. 3b). Within the rim zone, there are local subgrain boundaries. At the margin of the titanite megacryst, there is a zone rich in rutile inclusions (verified by Raman spectroscopy) that probably formed at the expense of the titanite megacryst (Fig. 3c) by the reaction titanite + CO_2 = rutile + calcite(aragonite) + quartz(coesite).

The rutile grains show shape-preferred orientation parallel to the external foliation indicating growth during the early deformation stages. A second titanite generation overgrew this inclusion-rich zone at the rim of the megacryst. Concave titanite and convex calcite phase boundaries suggest that this renewed titanite growth occurred during annealing (Fig. 3c).

A third titanite generation occurs within the calcite matrix. These small hypidiomorphic titanite grains are characterized by significantly higher Al_2O_3 contents (6.4–7.2 wt.%, Fig. 3b) than the titanite megacryst and its recrystallized rims. Commonly, matrix titanite shows inclusions of rutile. Thus, crystallization of matrix titanite occurred during decompression (rutile + calcite(aragonite) + quartz(coesite) = titanite + CO_2), probably still syn-deformational under UHP conditions.

Titanite that grew during subduction and during exhumation differ in initial Sr and Nd isotopic composition (Table 1) and in chemical composition (Fig. 3b). U–Pb dating of these two titanite generations constrains the time frame of subduction and exhumation and

Fig. 3. Petrologic and isotopic data for calcsilicate sample 9864. (a) *PT*-path (modified after Schmid, 2001 and Carswell et al., 2000) showing the likely growth conditions for pre-UHP titanite and matrix titanite. Mineral abbreviations according to Kretz (1983). The position of the titanite forming reaction depends on XCO_2 and is shown for $XCO_2 = 0.001$; higher XCO_2 shifts the curve to higher temperatures. (b) Megacryst (closed diamonds) and matrix (open squares) titanite show significant differences in chemical composition. The megacryst, which crystallized at LP/MP during prograde metamorphism, has lower Al contents than the high aluminous HP matrix titanite. For comparison, titanite from sample 9834 (titanite in phengite and syn-deformational matrix titanite) are shown for comparison. (c) The pre-UHP titanite megacryst (bottom) shows a rutile-rich zone that formed during deformation at high pressures. Rutile from this zone is overgrown by titanite (upper left) during annealing at medium grade. Photo is ca. 0.2 mm wide, parallel nicols. (d) Phengitic white mica and coarse calcite grains show shape preferred orientation. Within the calcite matrix concave/convex grain boundaries (upper left) and elongated grain shapes indicate mass transfer by diffusion creep (see text). Photo is ca. 0.4 mm wide, parallel nicols. (e) Concordia diagram for nine samples taken along a profile through the titanite megacryst. There are no systematic changes between core and rim. The matrix titanite has completely different isotopic ratios (Table 2). (f) Rb–Sr diagram for phengite, biotite, and calcite. Phengite yields a two-point age of 227 ± 5 Ma. Low initial $^{87}Sr/^{86}Sr$ values (0.704) are consistent with Sr from other marbles of the Changpu area (Romer et al., 2003). In more silicic marbles, initial $^{87}Sr/^{86}Sr$ ratios are as high as 0.708. Arrow in inset indicates the position titanite megacryst.

brackets events of extensive strain, metasomatism, and fluid infiltration into marble during exhumation from UHP to mid-crustal conditions.

3.1.2. Deformation of the calcsilicates

Calcsilicates deformed at high pressure by dislocation creep that was followed by static annealing. The

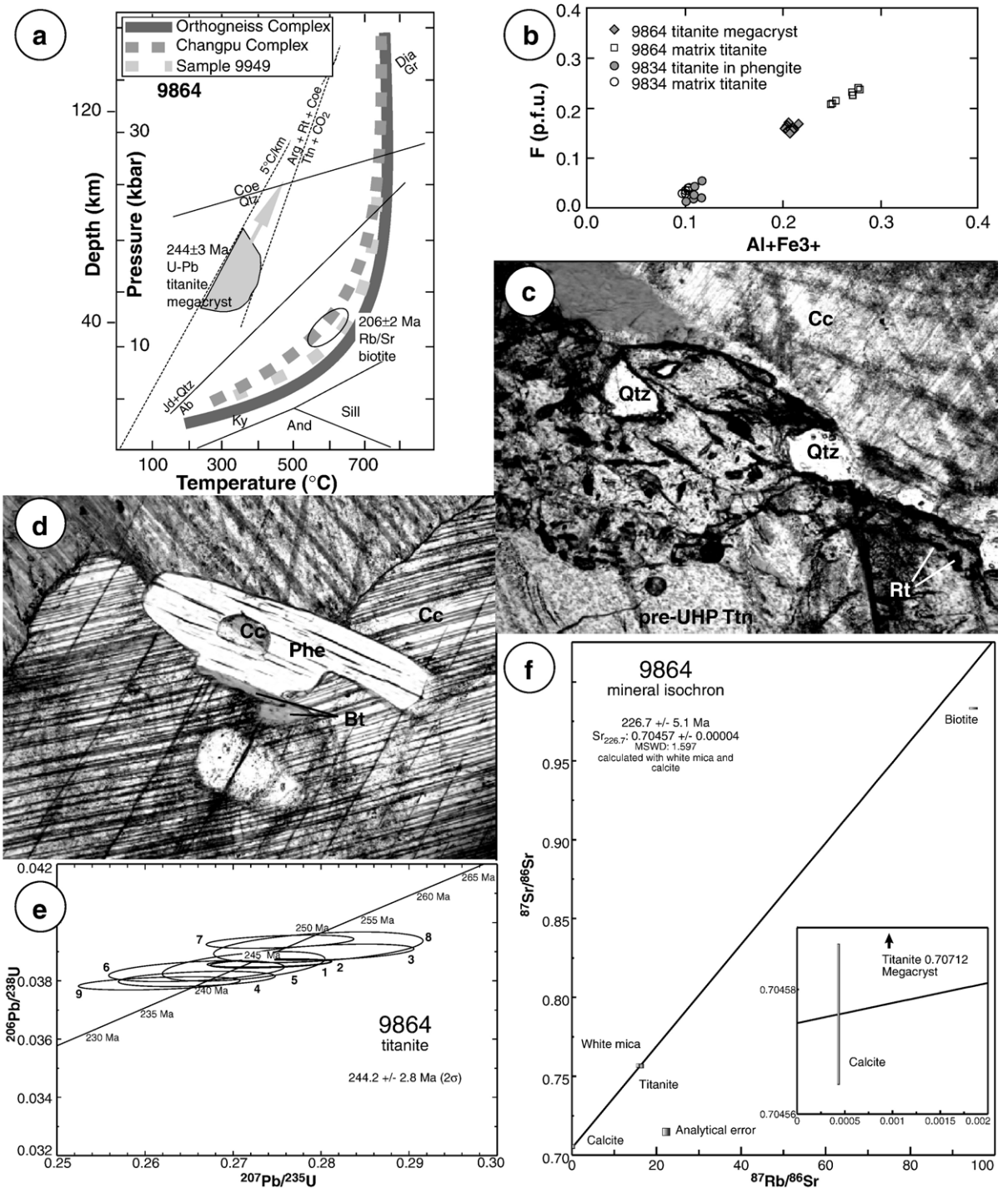

Table 1
Rb–Sr and Sm–Nd isotope data for a profile across a prograde titanite megacryst in marble 9864, Changpu area, Central Dabie Complex, Eastern China

Sample	Rb[a] (ppm)	Sr[a] (ppm)	$^{87}Sr/^{86}Sr$[b]	$^{87}Sr/^{86}Sr$[c]	Sm[a] (ppm)	Nd[a] (ppm)	$^{147}Sm/^{144}Nd$	$^{147}Nd/^{144}Nd$[b]	ε_{Nd}[d]
1	0.35	130.8	0.707189 ± 10	0.70716		912		0.511887	
2	0.088	131.1	0.707217 ± 10	0.70721		902		0.511875	
3	0.11	131.9	0.707257 ± 7	0.70725	262	934	0.1698	0.511886	−13.8
4	0.13	129.7	0.707310 ± 7	0.70730	269	971	0.1678	0.511898	−13.5
5	0.38	135.3	0.707327 ± 7	0.70730	234	864	0.1637	0.511868	−14.0
6	0.65	140.3	0.707446 ± 7	0.70740	234	849	0.1662	0.511876	−13.9
7	0.32	136.0	0.707611 ± 7	0.70759	236	861	0.1656	0.511861	−14.2
8	0.16	130.5	0.707276 ± 11	0.70726	249	884	0.1705	0.511878	−14.0
9	0.45	141.1	0.707109 ± 7	0.70708	230	801	0.1736	0.511887	−13.9

[a] Concentration determined by isotope dilution.
[b] Analytical uncertainties of the individual measurements are reported as $2\sigma_m$ $^{87}Sr/^{86}Sr$ data are normalized with $^{87}Sr/^{86}Sr=0.1194$. $^{143}Nd/^{144}Nd$ data are normalized with $^{146}Nd/^{144}Nd=0.7219$.
[c] Recalculation of $^{87}Sr/^{86}Sr$ (T) to 240 Ma using λ $^{87}Rb=1.42E-11$ y^{-1}.
[d] Nd (T) calculated for 240 Ma using λ $^{147}Sm=6.54E-12$ y^{-1}, $(^{147}Sm/^{144}Nd)^0$ CHUR=0.1967, and $(^{143}Nd/^{144}Nd)^0$ CHUR=0.512638.

microfabrics suggest the following crystallization history: Characteristic microfabrics in calcsilicate 9864 include locally elongated mineral aggregates of anorthite, biotite, clinozoisite, and rare titanite. These aggregates may be pseudomorphs after deformed garnet and reflect an early deformation increment probably at UHP conditions. The decomposition of garnet and the associated growth of titanite occurred at the static annealing stage during decompression. High-Al titanite within the calcite matrix had also formed at this stage. Carbonate forms a strain supporting framework consisting of a coarse grained calcite mosaic (300–500 μm) that resulted from static grain growth (annealing) overprinting the syn-deformational carbonate crystals, that must have been aragonite. Accordingly, the calcite grains do not show features of intracrystalline deformation. Only locally, there is microtextural evidence, such as concave/convex grain boundaries and absence of 120° triple points (Fig. 3d) and distinctly elongated, but internally strain-free, grains for deformation by dissolution precipitation creep. This may correlate with deformation under amphibolite facies conditions. Abundant mechanical twinning formed during later stages.

Large phengite crystals (350 μm) crystallized during deformation, and show shape-preferred orientation parallel to the mineral aggregates. They lack a distinct compositional zoning and have a high Si content (3.6 Si p.f.u.), which is consistent with UHP metamorphism (Hermann, 2003; Massonne and Szpurka, 1997) and deformation of this rock together with the neighbouring metasedimentary rocks. These metasedimentary rocks have been shown to contain coesite and jadeite (Carswell et al., 1996; Schmid, 2001). Probably, rutile formation from the titanite megacryst also occurred during UHP metamorphism. However, due to the lack of garnet formation in association with rutile, no precise *PT*-evaluation is possible.

Locally, phengite intergrown with biotite demonstrates decomposition of phengite during decompression (Fig. 3d). Such phengite varies in Si-content from 3.4 (core) to 3.3 Si p.f.u. (rim) with patches of even lower Si content (3.2 p.f.u.). Biotite growth is essentially static, implying that the deformation must have occurred at high pressure.

3.1.3. U–Pb data

The U–Pb system of titanite is able to survive temperatures substantially higher than 700 °C, depending on grain size and cooling rates, without experiencing Pb-loss by volume diffusion (Frost et al., 2000). For instance, Romer and Rötzler (2001, 2003) found titanite that remained a closed system with respect to the U–Pb system at temperatures as high as 1050 °C. Since titanite may form by several different reactions involving a wide rage of precursor minerals, it may have a heterogeneous initial Pb isotopic composition, which could induce excess scatter among the age data and yield too old ages if a precursor mineral had radiogenic Pb (cf. Romer, 2001; Romer and Rötzler, 2003).

Textural relationships suggest that the titanite megacryst grew during the prograde (burial) stage long before peak pressure was reached (Fig. 3a). We analyzed nine samples that were cut along a profile across the megacryst (Fig. 4). The margin with post-peak rutile and abundant annealing textures could not be sampled.

The samples have U contents between ca. 216 and 288 ppm, and Pb contents between ca. 16 and 21 ppm (Table 2). The blank corrected $^{206}Pb/^{204}Pb$ values of all nine samples range between ca. 110 and 120. The

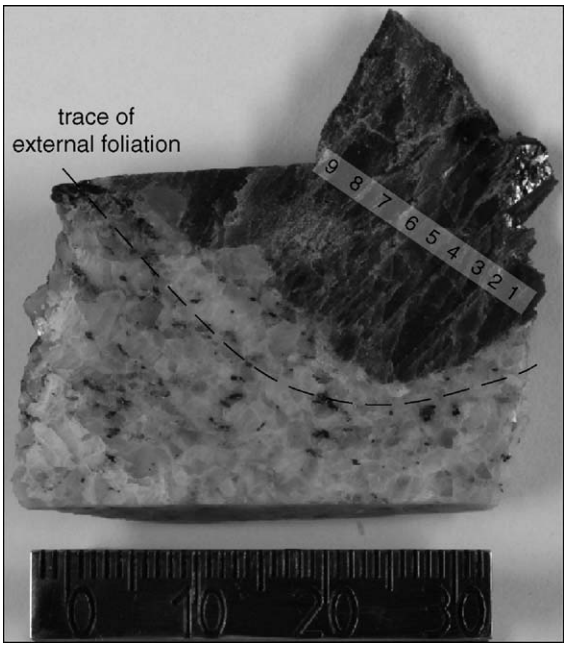

Fig. 4. Pre-UHP titanite megacryst in calcsilicate (sample 9864). Profile shows the location of the nine samples used for U–Pb dating. Scale bar in mm.

$^{238}U/^{204}Pb$ ratios of ca. 2400–2700 are significantly higher compared to those from titanite of nearby quartzofeldspathic samples (ca. 100). Nevertheless, since the proportion of common lead is about 30% of the total Pb, the choice of initial lead isotopic composition will affect the apparent $^{206}Pb/^{238}U$ ages, and the position of data points in a concordia diagram. The initial Pb isotopic composition is not accessible for analysis as the matrix calcite had recrystallized and behaved as an open system after the formation of the titanite megacryst. Therefore, the common lead correction may be based on the regression of the nine samples in $^{206}Pb/^{204}Pb$ vs. $^{238}U/^{204}Pb$ and $^{207}Pb/^{204}Pb$ vs. $^{235}U/^{204}Pb$ diagrams. Since these regression lines could represent rotated mixing lines and define incorrect values for the initial Pb, we tested whether the titanite megacryst is likely to have had a homogenous initial Pb isotopic composition by analyzing (i) the isotopic composition of Sr and Nd, which reflects the contribution from different precursor minerals, and (ii) the chemical composition, which shows the combined effect of formation conditions and availability of substituting ions (e.g., Fe, Al, F; Fig. 3b). The Sr and Nd isotopic compositions (and chemical composition) vary only slightly within the titanite megacryst and are fundamentally different from titanite in the calcite matrix (Tables 1 and 3). This suggests that Pb is likely to have been isotopically homogeneous and that the U–Pb system of the titanite megacryst remained closed. Calcite in the matrix changed its Sr isotopic composition after titanite crystallisation. Marble samples from the Central Dabie Complex show a systematic variation from crustal $^{87}Sr/^{86}Sr$ values to mantle-like $^{87}Sr/^{86}Sr$ values, which have been interpreted to reflect fluid infiltration during UHP metamorphism (Romer et al., 2003). The Sr isotopic composition of these marbles correlates with the Pb isotopic composition, the samples with the least radiogenic $^{87}Sr/^{86}Sr$ having the highest $^{206}Pb/^{204}Pb$ (Romer, unpubl. data). Initial titanite Pb has been corrected using a Pb isotopic composition that corresponds in the Pb–Sr isotopic variation trend to a $^{87}Sr/^{86}Sr$ of 0.70719–0.70761. The use of a more radiogenic initial Pb would reduce the $^{206}Pb/^{238}U$ age no more than 1–2 Ma.

All fractions yield concordant data that fall in the $^{206}Pb/^{238}U$ age range between 240 and 250 Ma (Fig. 3e). If the titanite megacryst showed closed system behaviour during UHP and subsequent metamorphic overprint, the ages would put an age constraint on the progressive metamorphic stage. We consider the weighted mean $^{206}Pb/^{238}U$ age of 244 ± 3 Ma a conservative estimate for titanite formation and, thus, the maximum age constraint for UHP metamorphism. This age of titanite agrees well with the slightly younger U–Pb monazite and zircon and Ar–Ar phengite age data attributed to UHP metamorphism (Hacker et al., 2000; Ayers et al., 2002). In agreement with our titanite age, Li et al. (2004) reported an U–Pb zircon age of 242 ± 3 Ma for the onset of peak pressure and interpreted Ar–Ar paragonite data of 246 ± 10 and 241 ± 3 Ma as mineral crystallization during prograde metamorphism.

Matrix titanite is less radiogenic and yields a younger apparent age than the titanite megacryst, which corroborates with the late stage nature of matrix titanite. The U–Pb isochron diagram indicates that the initial Pb isotopic composition of matrix titanite, calcite, clinozoisite and other matrix phases may have been heterogeneous. The small range in $^{238}U/^{204}Pb$ values precludes a precise age determination. For matrix titanite, the apparent $^{206}Pb/^{238}U$ age for the clinozoisite–titanite pair is 214 ± 4 Ma (2σ), whereas the apparent $^{206}Pb/^{238}U$ age for the calcite–titanite pair is 209 ± 7 Ma (2σ). Whether either of these apparent ages has geologic significance depends on the initial Pb isotopic composition of the used minerals.

3.1.4. Rb–Sr analyses

Rb–Sr analyses were made from calcite, phengite, biotite, and the titanite megacryst. The low $^{87}Sr/^{86}Sr$ value (0.70457, Table 3) of the marble contrasts with markedly more radiogenic $^{87}Sr/^{86}Sr$ values (0.70711–

Table 2
U–Pb data of calcsilicate sample 9864 (subsamples of the titanite megacryst, matrix titanite, calcite and clinozoisite) and gneissic migmatite sample 9949 (titanite and epidote) from the Central Dabie Complex

Sample	Sample weight [mg]	Concentrations		Corrected ratios[a]			Calculated ratios[b]				Apparent ages [Ma][c]		
		U [ppm]	Pb [ppm]	$^{206}Pb/^{204}Pb$	$^{207}Pb/^{204}Pb$	$^{208}Pb/^{204}Pb$	$^{238}U/^{204}Pb$	$^{206}Pb/^{238}U$	$^{207}Pb/^{235}U$	$^{207}Pb/^{206}Pb$	$^{206}Pb/^{238}U$	$^{207}Pb/^{235}U$	$^{207}Pb/^{206}Pb$
9864													
9864.1 titanite	0.457	274	18.7	118.74	20.85	67.22	2627	0.0386	0.274	0.0515	244	246	262
9864.2 titanite	0.447	265	18.2	117.67	20.80	67.31	2600	0.0386	0.274	0.0515	244	246	265
9864.3 titanite	0.744	240	17.6	109.90	20.47	70.46	2375	0.0390	0.281	0.0523	247	252	299
9864.4 titanite	0.435	283	18.8	120.26	20.85	66.52	2705	0.0381	0.266	0.0507	241	239	225
9864.5 titanite	1.232	216	15.6	110.09	20.37	70.59	2410	0.0385	0.271	0.0511	244	244	245
9864.6 titanite	0.617	288	19.8	120.02	20.80	71.52	2680	0.0383	0.266	0.0503	242	239	209
9864.7 titanite	0.743	270	19.1	119.39	20.81	71.35	2595	0.0393	0.275	0.0508	249	247	230
9864.8 titanite	0.746	297	20.9	119.62	20.93	71.83	2614	0.0391	0.280	0.0518	248	250	278
9864.9 titanite	0.485	278	19.0	117.52	20.65	69.89	2644	0.0379	0.262	0.0501	240	236	198
9864.10 matrix-titanite	0.214	49.7	8.29	37.88	16.73	43.02	509.9	0.0330	0.188	0.0414	209	175	
9864 calcite	0.716	0.0547	10.9	21.12	16.04	39.25	0.290						
9864 clinozoisite	0.622	0.15	0.63	21.11	15.90	39.01	15.86						
9949													
9949.1 titanite	0.253	87.3	54.9	20.76	15.60	38.26	104	0.0378	0.325	0.0624	239	286	689
9949.2 titanite	0.608	86.9	54.3	20.76	15.59	38.11	104	0.0375	0.307	0.0594	238	272	581
9949.3 titanite	0.671	94.0	61.9	20.53	15.60	38.18	98.7	0.0373	0.332	0.0645	236	291	759
9949.4 epidote	0.871	13.1	200	17.00	15.37	37.56	4.02	0.0396			250		
9949.5 epidote	1.344	18.5	328	16.97	15.38	37.60	3.45	0.0362			229		
9949.6 epidote	0.911	15.0	343	16.94	15.36	37.51	2.67	0.0372			235		
9949.7 epidote	0.556	14.7	270	16.97	15.36	37.52	3.33	0.0384			243		

[a] Lead isotope ratios corrected for 0.1% per a.m.u. fractionation, 15 pg Pb blank, isotopic tracer, and initial lead.

[b] U corrected for 0.1% per a.m.u. fractionation and 1 pg U blank. A ^{205}Pb–^{235}U mixed tracer was used to determine the various Pb/U ratios. All uncertainties were calculated taking into consideration measurement errors, 30% uncertainty for the fractionation correction, 50% uncertainty for the blank level and uncertainties for the common Pb composition as shown below and comparable uncertainties for blank Pb composition. The uncertainty of $^{205}Pb/^{235}U$ in the tracer is less than 0.3%. Data reduction was performed by Monte Carlo modelling of 1000 random normally distributed data sets that fit above uncertainty limits, allowing for error correlation when appropriate. Uncertainties of $^{206}Pb/^{238}U$, $^{207}Pb/^{235}U$, and $^{207}Pb/^{206}Pb$ range from 0.5–1.7%, 2.3–3.8%, and 2.0–3.5%, respectively, but for the U-poor titanite from sample 9949. These uncertainties of $^{207}Pb/^{235}U$ and $^{207}Pb/^{206}Pb$ of 10–12%, and the error correlation between $^{206}Pb/^{238}U$ and $^{207}Pb/^{235}U$ of 0.4–0.6 largely depend on the measured $^{206}Pb/^{204}Pb$.

[c] Apparent ages were calculated using the decay constants for U and Th recommended by IUGS (Steiger and Jäger, 1977) and initial lead isotopic compositions: $^{208}Pb:^{207}Pb:^{206}Pb:^{204}Pb = 37.2:15.5:17.3:1$, for sample 9864.1 to 9864.9, and calcite compositions 39.22:16.03:21.07:1 for sample 9864.10, resp.; $^{208}Pb:^{207}Pb:^{206}Pb:^{204}Pb = 37.5 \pm 0.06:15.4 \pm 0.01:16.8 \pm 0.01:1$ for sample 9949.

0.70759, Table 1) of the prograde titanite megacryst. Since titanite carries essentially no Rb and its initial Sr-isotopic composition is determined by the phases consumed during titanite growth, the relatively homogeneous initial $^{87}Sr/^{86}Sr$ of titanite and its more radiogenic composition than the marble–Sr implies: (i) During titanite growth, there was no significant change in precursors, as otherwise their Sr (and Nd) isotopic composition (Table 1) would have been more variable; (ii) calcite, the major Sr carrier, was inert during titanite growth or – more likely – changed its Sr isotopic composition during later fluid-infiltration and recrystallization (cf. Romer et al., 2003). The phengite sample consists of a few large grains without biotite rims. This fraction contains predominantly unzoned phengite with a Si content of 3.6 p.f.u., corresponding to UHP conditions (Hermann, 2003). The Rb–Sr phengite–calcite age (227 ± 5 Ma) represents the age for phengite crystallization if phengite formed after calcite had acquired its unradiogenic Sr. This age, however, will be slightly too old if phengite formed before calcite acquired its low $^{87}Sr/^{86}Sr$.

The biotite–calcite age is 206 ± 2 Ma. As fluid infiltration and alteration of the Sr isotopic composition in calcite (Romer et al., 2003) occurred at higher pressures than biotite growth, the obtained age dates biotite growth during retrograde metamorphism (at rather high pressures). Consistently, in this sample, both mica ages are significantly older than mica ages from quartz feldspar gneisses.

Table 3
Rb–Sr data of samples 9864 (calcsilicate), 9949 (gneissic migmatite), 9834 (orthogneiss deformed as HT), 99101 and 9837 (gneissic eclogite), 99105 and 99104 (gneisses from localized shear zones) from the Central Dabie Complex

Sample no.	Sample	Rb [ppm][a]	Sr [ppm][a]	$^{87}Rb/^{86}Sr$	$^{87}Sr/^{86}Sr$	$\pm 2\sigma_m$
9864.1	Biotite	245	7.7	94.9	0.98295	0.00001
9864.2	White mica	241	42.9	16.3	0.75658	0.00001
9864.3	White mica	235	42.9	16.0	0.75660	0.00001
9864.4	Calcite	0.2	1571	0.00	0.70458	0.00001
9864.5	Titanite megacryst	0.1	128.8	0.00	0.70712	0.00001
9949.1	Biotite	406	6.8	180.5	1.18659	0.00003
9949.2	White mica	260	15.2	50.3	0.85137	0.00001
9949.3	Feldspar	54.6	339.0	0.47	0.71281	0.00001
9949.4	Epidote	4.0	4957	0.00	0.71166	0.00001
9834.1	White mica	245	152.7	4.65	0.72275	0.00004
9834.2	White mica	234	93.3	7.27	0.73089	0.00001
9834.3	White mica	97.2	407.0	12.1	0.73029	0.00004
9834.4	Whole rock	46.1	5182	0.03	0.70945	0.00004
9834.5	Feldspar	30.2	860.5	0.10	0.70953	0.00001
9834.6	Feldspar	28.1	849.4	0.10	0.70953	0.00001
9834.7	Clinozoisite	3.1	8177	0.00	0.70936	0.00001
9834.8	Clinozoisite	0.7	6499	0.00	0.70942	0.00001
9834.9	Titanite	1.7	422.7	0.01	0.70771	0.00001
99101.1	White mica	289	142.4	5.89	0.73168	0.00001
99101.2	Whole rock	75.6	133.3	1.64	0.71835	0.00001
99101.3	Clinopyroxene	16.0	146.7	0.32	0.71426	0.00001
99101.4	Clinopyroxene	0.1	122.9	0.00	0.71426	0.00001
9837.1	White mica	290	283.3	2.96	0.72229	0.00004
9837.2	White mica	284	285.2	2.88	0.72230	0.00004
9837.3	Whole rock	74.6	135.7	1.59	0.71784	0.00004
9837.4	Epidote	22.5	1574	0.04	0.71375	0.00001
9837.5	Clinopyroxene	9.9	71.2	0.40	0.71489	0.00001
9837.6	Clinopyroxene	5.7	62.7	0.26	0.71471	0.00001
9837.7	Feldspar	0.1	0.5	0.50	0.71582	0.00003
99104.1	Biotite	360	2.3	512	2.01513	0.00024
99104.2	White mica	337	88.0	11.1	0.74812	0.00002
99104.3	White mica	334	88.0	11.0	0.74779	0.00001
99104.4	Whole rock	97.4	204.5	1.38	0.71855	0.00001
99104.5	Epidote	1.5	462.5	0.01	0.71504	0.00001
99104.6	Feldspar	0.1	1.5	0.24	0.71712	0.00004
99105.1	Biotite	413	1.6	918	3.05385	0.00072
99105.2	Whole rock	111	92.7	3.47	0.72492	0.00001
99105.3	Whole rock	110	3.3	96.6	0.67033	0.00001
99105.4	Epidote	4.7	303.6	0.04	0.71663	0.00001
99105.6	Feldspar	0.1	1.4	0.26	0.71937	0.00001

[a] Concentrations were determined by isotope dilution and mixed ^{87}Rb–^{84}Sr tracers.

3.2. Decompressional partial melting and HT deformation (gneissic migmatite of the Orthogneiss Complex)

Sample 9949 is a leucocratic granoblastic white mica–biotite–plagioclase–K-feldspar gneiss. This gneiss occurs close to the boundary between Central Dabie Complex and North Dabie Complex, the Wuhe Shuihou Fault (after Bryant et al., 2004). Like many quartzofeldspathic rocks from the Orthogneiss Complex, this sample has been intensively deformed at high temperature during decompression (Fig. 5a). It does not show any mineralogical evidence for the UHP stage. Large epidote grains (partly with hypidiomorphic allanite/clinozoisite core, Fig. 5d), idiomorphic titanite, and abundant microcline suggest crystallization of these minerals from a partial melt or from fluids, consistent with the decompression *PT*-path being within the partial melting domain of wet granitic crust. The gneiss shows a three stage history, whereby the older stages (i) and (ii) are preserved in microlithons that are not affected by the younger deformation (e.g. Bard, 1986): (i) partial melting is followed by (ii) strain accumulation and grain growth at low differential stresses and high temperature (about 600 °C or higher, Vernon, 1999). Subgrain boundaries in

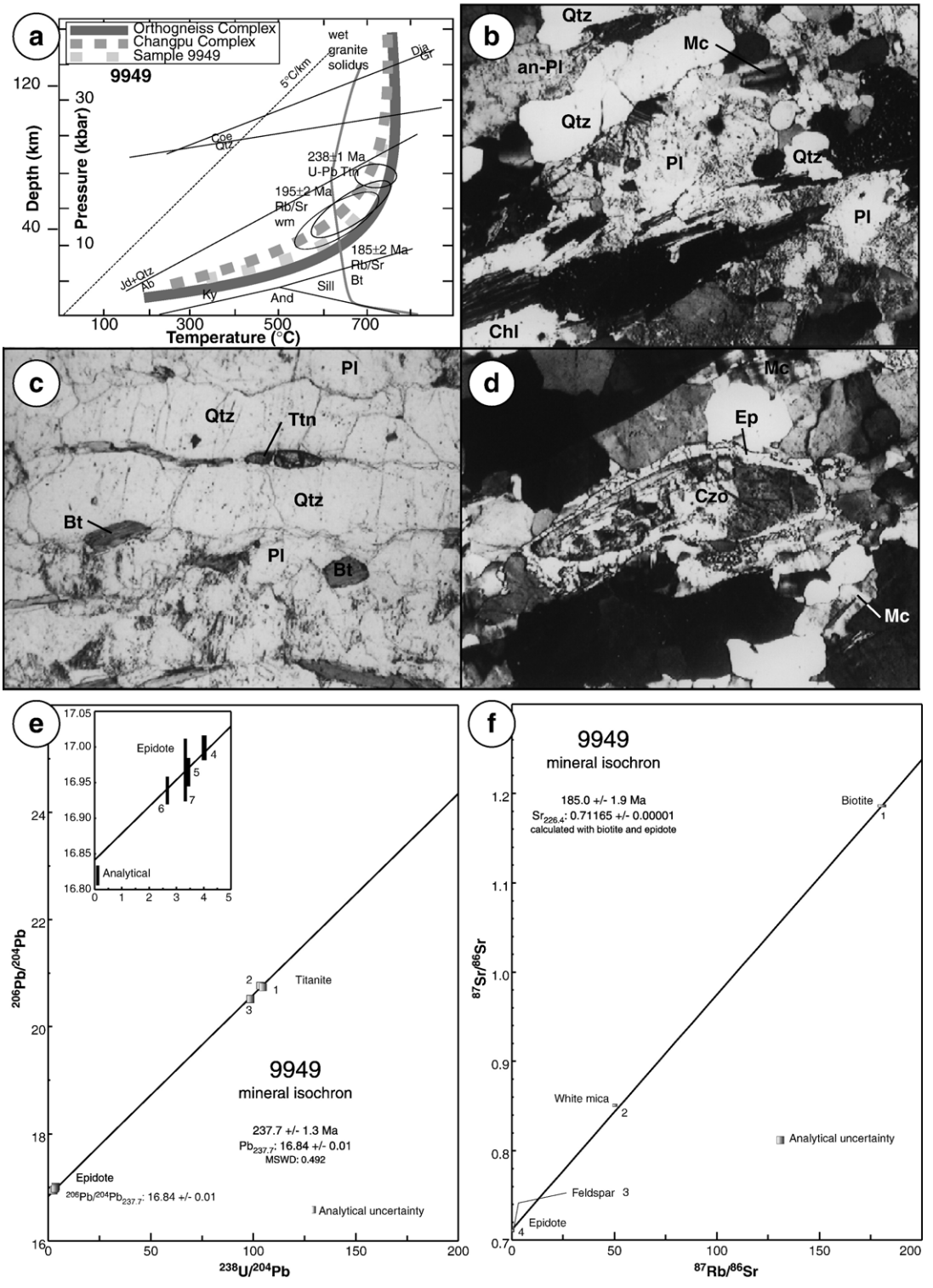
a
Orthogneiss Complex
Changpu Complex
Sample 9949
9949
wet granite solidus
Dia
Gr
5°C/km
Coe
Qtz
238±1 Ma U-Pb Ttn
195±2 Ma Rb/Sr wm
185±2 Ma Rb/Sr Bt
Jd+Qtz
Ab
Ky
And
Sill
Depth (km)
Pressure (kbar)
Temperature (°C)
b
Qtz
Mc
an-Pl
Qtz
Pl
Qtz
Pl
Chl
c
Pl
Qtz
Ttn
Qtz
Bt
Pl
Bt
d
Mc
Ep
Czo
Mc
e
Epidote
Analytical
Titanite
9949
mineral isochron
237.7 +/- 1.3 Ma
Pb237.7: 16.84 +/- 0.01
MSWD: 0.492
Epidote
206Pb/204Pb237.7: 16.84 +/- 0.01
Analytical uncertainty
206Pb/204Pb
238U/204Pb
f
9949
mineral isochron
185.0 +/- 1.9 Ma
Sr226.4: 0.71165 +/- 0.00001
calculated with biotite and epidote
Biotite
White mica
Feldspar
Epidote
Analytical uncertainty
87Sr/86Sr
87Rb/86Sr

feldspar, bulging of new feldspar grains, concave/convex grain boundaries (lack of equilibrium grain boundary configurations), and inhomogeneous grain size distribution demonstrate that dissolution precipitation creep (diffusion creep) was the predominant deformation mechanism. Shape-preferred orientation of slightly elongated feldspar grains and of grain boundaries define a weak foliation plane (Fig. 5b). Abundant quartz inclusions in K-feldspar result from recrystallized myrmekite. Microshear zones of a younger deformation stage (iii) are concentrated into white mica–biotite–quartz, feldspar–quartz, and pure quartz domains surrounding the microlithons. Locally, biotite decomposed during cooling to chlorite and ilmenite.

Within the microlithons, relics of white mica are oriented within the foliation plane and form symplectitic intergrowth with K-feldspar and biotite that formed at the expense of older phengite. The white mica relics show a Si component of 3.3 p.f.u., consistent with a crystallization pressure of ca. 18 kbar (see discussions in Hermann, 2003; Massonne and Szpurka, 1997). The stability of plagioclase sets an upper pressure limit of 20 kbar at the given temperature. This rather narrow pressure bracket is interpreted to either reflect the conditions of crystallization from a partial melt, or, more likely, a solidus reaction after crystallization of the melt. The white mica formed from an older phengite with higher Si that formed at HP.

3.2.1. U–Pb data

Idiomorphic titanite shows shape preferred orientation parallel to the microlithons' foliation plane and is locally fractured (Fig. 5c). Epidote megacrysts (with an allanite/clinozoisite core) show undulatory extinction (Fig. 5d). Local subgrain boundaries within epidote show that titanite and epidote, which had crystallized from the melt, remained stable during deformation. There is no rutile. The mineral paragenesis restricts *P–T* conditions during melt crystallization and deformation below the pressure-sensitive titanite-forming reaction anorthite + titanite + V = clinozoisite + rutile + quartz, which may occur at $P > 15$ kbar, at T ca. 700 °C, assuming $XCO_2 = 0.1$ (Ye et al., 2002; Holland and Powell, 1990).

Titanite and epidote are considered to be cogenetic and to belong to a single generation. Epidote overgrowth on allanite reflects continuous crystallization from a partial melt progressively more depleted in REE (cf. also Romer and Xiao, 2005). Because of the unradiogenic Pb isotopic composition of titanite and epidote (Table 2), the age was determined from an isochron in the $^{206}Pb/^{204}Pb$ vs. $^{238}U/^{204}Pb$ diagram (Fig. 5e). ^{238}U–^{206}Pb isochron dating is advantageous for samples with low $^{206}Pb/^{204}Pb$ ratios, because no estimate for the initial Pb isotopic composition is required. In this sample, titanite yields $^{206}Pb/^{204}Pb$ blank corrected ratios of only ca. 21. Three titanite fractions yield a $^{206}Pb_{rad}/^{238}U$ value of ca. 0.038, which corresponds to an apparent age of 236–239 Ma (Table 2). The regression line defined by epidote–titanite data in the $^{206}Pb/^{204}Pb$ vs. $^{238}U/^{204}Pb$ diagram corresponds to an age of 238 ± 1 Ma (2σ; Fig. 5e) with an initial $^{206}Pb/^{204}Pb$ of 16.84 ± 0.01.

This epidote–titanite $^{206}Pb/^{238}U$ age represents a robust age constraint for crystallization from a partial melt, being homogenous in its initial Pb isotopic composition, during a first rapid exhumation to amphibolite facies conditions. As crystallization occurred from the partial melt at a pressure of ca 18–20 kbar (Fig. 5a), this age constrains the emplacement of this UHP rock at a depth corresponding to 18–20 kbar.

Interestingly, this age falls within the age range obtained for UHP metamorphism (Ayers et al., 2002; Liu et al., 2004a,b; Li et al., 2004), thus indicating polychronous UHP metamorphism and uplift. Crystallization ages of strongly deformed potassium feldspar-rich dikes (partial melts) from the Sulu UHP terrain overlap with the age of peak UHP metamorphic conditions, also implying the presence of melt during metamorphism and exhumation (Wallis et al., 2005).

Fig. 5. Quartzofeldspathic gneiss from the Changpu area (sample 9949). (a) *PT*-path showing the likely conditions for the HT metamorphic episode characterized by decompressional partial melting and growth of titanite and associated minerals. Wet granite solidus curve after Stern and Wyllie (1981). Mineral abbreviations according to Kretz (1983). (b) Microfabrics of the microlithons show that high-temperature deformation in the quartzofeldspathic rocks was mostly accommodated by diffusion precipitation creep. This is indicated by elongated quartz and feldspar grains, grain shape orientation, and a distinct lack of equilibrium grain boundary configurations (no 120° triple junctions, no straight, but concave/convex grain boundaries). Photo is ca. 2.3 mm wide, crossed nicols. (c) Syn-deformational titanite between elongated quartz and feldspar domains showing characteristics of grain boundary migration (elongated grains internally strain free, lack of equilibrium grain boundaries). Photo is ca. 0.4 mm wide, parallel nicols. (d) Within the microlithons, predeformative epidote megacrysts (partly with clinozoizisite core) show locally undulatory extinction. Photo is ca. 1.2 mm wide, crossed nicols. (e) ^{238}U–^{206}Pb isochron diagram showing two data clusters defined by three titanite and four epidote samples, respectively, yielding 238 ± 1 Ma. (f) Rb–Sr isochron diagram for feldspar, epidote, white mica, and biotite – illustrating in agreement with the multistage deformation history – the isotopic heterogeneity among the mineral phases.

3.2.2. Rb–Sr analyzes

The Rb–Sr systematics of this rock (Fig. 5f, Table 3) shows significant scatter that either implies the initial Sr isotopic heterogeneity between epidote, white mica, feldspar, and biotite or reflects a multistage crystallization and deformation history (microlithons and microshear zones).

The Rb–Sr ages of 195 ± 2 Ma (2σ) for white mica and 185 ± 2 Ma (2σ) for biotite are obtained independently whether feldspar or epidote is used to constrain the low-$^{87}Sr/^{86}Sr$ member of the two-point isochron. Special care was taken to analyze fractions of pure biotite (free of chlorite and ilmenite intergrowth) and white mica (Si content ca. 3.3 p.f.u.) to diminish the effect of mixing with less radiogenic or younger components. Since the incorporation of less radiogenic Sr would result in too young ages, the Rb–Sr mica ages yield minimum age constraints for exhumation and emplacement of this rock in the middle crust.

3.3. Subsequent episodes of HT deformation (Orthogneisses 9834, 99144)

The following two samples show subtle, though important differences in microfabrics that are the expression of particular structural positions. Sample 9834 has been deformed during cooling. Its fabrics are typical for rocks deformed close to a shear zone causing exhumation of (HP) rocks into a mid-crustal level. Sample 99144 is tempered as the result of slow cooling after deformation, typically for rocks distant from bounding shear zones. Since the internal structure of the Central Dabie Complex is poorly known, we discuss the two HT-gneisses from the Orthogneiss Complex separately, as they could belong to distinct subunits differing in the timing of their exhumation.

3.3.1. Sample 9834

Microfabrics of a clinozoisite–titanite bearing gneiss (sample 9834, Fig. 1) reveal fluid access and nearly complete re-equilibration at HT below the stability field of eclogite, succeeded by intense pervasive strain still at high temperatures (Fig. 6a). HT-deformation is constrained by quartz microfabrics, such as subgrain boundaries subnormal and subparallel to the trace of the crystallographic [*c*]-axis indicating activation of [*c*]-slip in quartz consistent with strain accumulation at subsolidus conditions (Berté et al., 1979; Gapais and Barbarin, 1986). However, quartz domains do not coalesce to a strain supporting framework and dissolution precipitation creep was the dominant deformation mechanism. Abundant microtectonic features characteristic for dissolution precipitation creep include elongated plagioclase and quartz crystals that are internally strain-free, concave/convex grain and phase boundaries, and the lack of equilibrium grain boundary configurations. Dissolution precipitation creep is an effective mechanism for isotopic exchange (Krohe and Wawrzenitz, 2000). This deformation overprinted an older deformation episode dominated by dislocation creep involving dynamic (re-)crystallization. This is indicated by the bimodal grain size distribution of clinozoisite, epidote, and mica. A shape preferred orientation of all minerals defines the foliation (Fig. 6b).

Larger minerals of clinozoisite-1, epidote-1, and phengitic white mica-1 reach 1–2 cm size. They are older than the mesoscopic foliation. The syn-deformational matrix domains are mainly composed of clinozoisite-2, An-plagioclase, epidote-2, and phengitic white mica-2 with a grain size not exceeding 1 mm. Typically, the Si content (ca. 3.3 p.f.u.) is identical for the two generations of phengitic white mica. Pre-deformative grains do not show compositional zoning. Pre- and syn-deformational grains have similar and homogeneous Si contents, suggesting crystallization of both under the same *PT*-conditions, may be in close temporal association. However, the lack of biotite and K-feldspar precludes a pressure estimation by phengite-barometry. Stability of clinozoisite (at the given T) evidences syn-deformational $P >$ ca. 10 kbar $<$ ca. 20 kbar, i.e., below the eclogite-stability field (Fig. 6a).

Titanite is syn-deformational with respect to the high temperature strain episode. There are two types of titanite, i.e., in the matrix and included in phengite

Fig. 6. Clinozoisite–titanite bearing gneiss (sample 9834). (a) *PT*-path showing the likely conditions for syn-deformational titanite and cogenetic mineral growth linked to a HT deformation episode. Mineral abbreviations according to Kretz (1983). (b) Gneiss is characterized by a high-*T* strain episode. The main mineral assemblage An-plagioclase, quartz, phengitic white mica, epidote, and clinozoisite shows preferred orientation of the elongated crystals parallel to the foliation. Idiomorphic titanite is also syn-deformational. Photo is ca. 2.3 mm wide, parallel nicols. (c) Shape preferred orientation of syn-deformational titanite parallel to the foliation as defined by phengite (upper part) and clinozoisite (lower part of the photograph). Photo is ca. 0.2 mm wide, parallel nicols. (d) Titanite inclusion (idiomorphic, center of photo) in pre-deformational clinozoisite. Clinozoisite is associated with phengitic white mica showing kinks. Photo is ca. 1.4 mm wide, parallel nicols. (e) ^{238}U–^{206}Pb multimineral isochron for mineral phases that define the macroscopic strain features. The age of 224 ± 2 Ma dates the HT deformation. (f) Rb–Sr isochron diagram for syn-deformational mineral phases that did not have a homogeneous initial Sr isotopic composition.

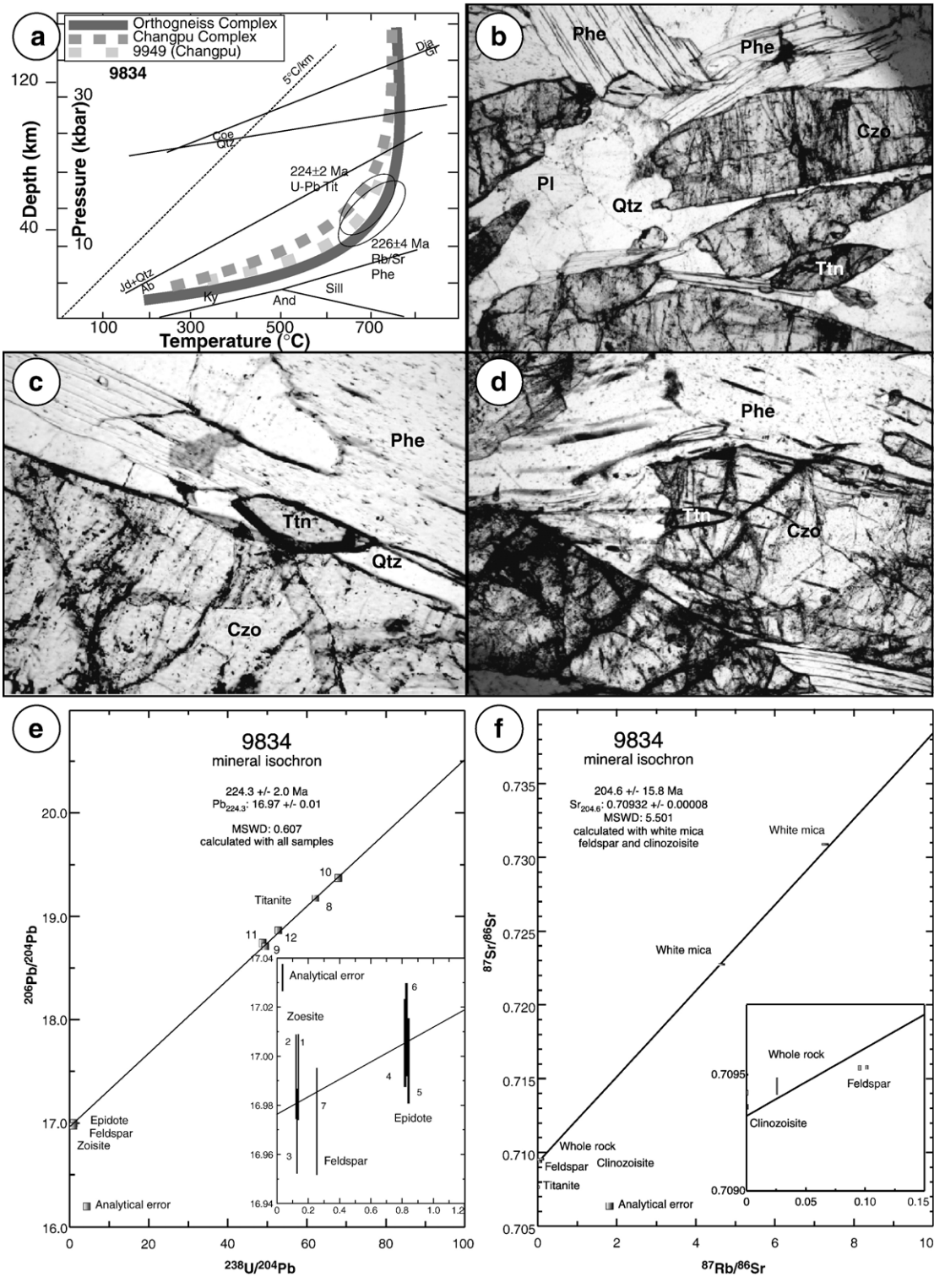
a
Orthogneiss Complex
Changpu Complex
9949 (Changpu)
9834
5°C/km
Dia
Gr
Coe
Qtz
224±2 Ma
U-Pb Tit
226±4 Ma
Rb/Sr
Phe
Jd+Qtz
Ab
Ky
And
Sill
Depth (km)
Pressure (kbar)
Temperature (°C)
b
Phe
Phe
Czo
Pl
Qtz
Ttn
c
Phe
Ttn
Qtz
Czo
d
Phe
Ttn
Czo
e
9834
mineral isochron
224.3 +/- 2.0 Ma
Pb224.3: 16.97 +/- 0.01
MSWD: 0.607
calculated with all samples
Titanite
Epidote
Feldspar
Zoisite
Analytical error
Zoesite
Feldspar
Epidote
206Pb/204Pb
238U/204Pb
f
9834
mineral isochron
204.6 +/- 15.8 Ma
Sr204.6: 0.70932 +/- 0.00008
MSWD: 5.501
calculated with white mica
feldspar and clinozoisite
White mica
White mica
Whole rock
Feldspar
Clinozoisite
Titanite
Analytical error
Whole rock
Feldspar
Clinozoisite
87Sr/86Sr
87Rb/86Sr

and clinozoisite. Since both kinds of titanite have crystallized in the same geochemical environment, their similar contents of F, Ti, Al, and Fe suggest that they had grown under the same *PT*-conditions (Fig. 6c). Titanite within the syn-deformational matrix had crystallized during shearing related to the early deformation episode (Fig. 6b). Titanite inclusions in large clinozoisite (Fig. 6d) and phengite crystals suggest continued growth of clinozoisite and phengite during later deformation, or after deformation, probably in close temporal association.

3.3.1.1. U–Pb data. U–Pb analyses were made from titanite, clinozoisite-1, epidote, and plagioclase. These minerals defining the macroscopic fabric had recrystallized under conditions when dissolution precipitation creep was the dominant deformation process. This process more effectively supports mixing and redistribution of elements over larger distances compared to dislocation creep (Krohe and Wawrzenitz, 2000). Titanite samples yield U contents between ca. 25 and 43 ppm, and Pb contents between ca. 32 and 44 ppm (Table 4). Pb of all samples is very unradiogenic. The blank corrected $^{206}Pb/^{204}Pb$ values range between 18.75 and 19.18 for the titanite samples and from 16.97 to 17.01 for clinozoisite, epidote, and feldspar samples.

In the $^{238}U/^{204}Pb$ vs. $^{206}Pb/^{204}Pb$ isochron diagram (Fig. 6e), all 12 analysed fractions from the clinozoisite–titanite bearing gneiss 9834 fall on a regression line. Provided closed system behavior and a common initial Pb isotopic composition of all mineral phases, its slope corresponds to an age of 224 ± 2 Ma and yields an initial $^{206}Pb/^{204}Pb$ ratio of 17.0.

A homogeneous initial Pb isotopic composition probably was supported by high-*T* metamorphism and deformation. The isochron consequently sets a time

Table 4
U–Pb data of orthogneiss samples 9834 and 99144, both deformed at HT, from the Central Dabie Complex

Sample	Sample weight	Concentrations		Corrected ratios[a]			Calculated ratios[b]		Apparent ages [Ma][c]
	[mg]	U [ppm]	Pb [ppm]	$^{206}Pb/^{204}Pb$	$^{207}Pb/^{204}Pb$	$^{208}Pb/^{204}Pb$	$^{238}U/^{204}Pb$	$^{206}Pb/^{238}U$	$^{206}Pb/^{238}U$
9834									
9834.1 clinozoisite	0.530	2.10	948	16.99	15.38	37.49	0.14		
9834.2 clinozoisite	1.015	1.81	911	16.99	15.38	37.49	0.12		
9834.3 clinozoisite	1.037	1.85	887	16.97	15.39	37.53	0.13		
9834.4 epidote	0.518	4.20	312	17.01	15.39	37.52	0.83		
9834.5 epidote	0.599	4.39	320	17.00	15.38	37.48	0.84		
9834.6 epidote	0.569	4.62	343	17.01	15.40	37.56	0.83		
9834.7 feldspar	0.664	0.09	22.2	16.97	15.38	37.49	0.26		
9834.8 titanite	0.497	43.1	44.0	19.18	15.51	37.84	62.2	0.0302	192
9834.9 titanite	0.551	34.7	44.0	18.71	15.49	37.72	49.6		
9834.10 titanite	0.454	45.4	42.6	19.38	15.52	37.88	68.0	0.0305	194
9834.11 titanite	0.361	24.9	32.1	18.75	15.51	37.82	49.0	0.0295	187
9834.12 titanite	0.505	31.1	37.1	18.86	15.47	37.74	52.9		
99144									
99144.1 titanite	0.816	111	19.2	32.13	16.14	38.50	438	0.0338	215
99144.2 titanite	0.509	104	18.6	31.66	16.23	38.78	422	0.0340	216
99144.3 epidote	0.155	42.4	291	17.48	15.43	37.71	9.03		
99144.4 garnet	1.138	0.22	0.49	17.90	15.29	37.34	27.3		
99144.5 garnet	0.795	1.40	6.22	17.76	15.57	38.05	14.1	0.0327	207

[a] Lead isotope ratios corrected for 0.1% per a.m.u. fractionation, 15 pg Pb blank, isotopic tracer, and initial lead.

[b] U corrected for 0.1% per a.m.u. fractionation and 1 pg U blank. A ^{205}Pb–^{235}U mixed tracer was used to determine the various Pb/U ratios. All uncertainties were calculated taking into consideration measurement errors, 30% uncertainty for the fractionation correction, 50% uncertainty for the blank level and uncertainties for the common Pb composition as shown below and comparable uncertainties for blank Pb composition. The uncertainty of $^{205}Pb/^{235}U$ in the tracer is less than 0.3%. Data reduction was performed by Monte Carlo modelling of 1000 random normally distributed data sets that fit above uncertainty limits, allowing for error correlation when appropriate. Uncertainties of $^{206}Pb/^{238}U$, $^{207}Pb/^{235}U$, and $^{207}Pb/^{206}Pb$ range from 0.35–0.76%, 0.44–0.82%, and 0.06–0.41%, respectively, but for the two U-rich samples. These uncertainties and the error correlation between $^{206}Pb/^{238}U$ and $^{207}Pb/^{235}U$ of 0.55–0.99 largely depend on the measured $^{206}Pb/^{204}Pb$.

[c] Apparent ages were calculated using the decay constants for U and Th recommended by IUGS (Steiger and Jäger, 1977) and initial lead isotopic compositions (see text): $^{208}Pb:^{207}Pb:^{206}Pb:^{204}Pb = 36.8:15.3:16.5:1$ for sample 9834; $^{208}Pb:^{207}Pb:^{206}Pb:^{204}Pb = 37.2:15.5:17.3:1$ for sample 99144.

constraint for HT deformation at *P–T* conditions below the eclogite (jd+grt) stability field, at $P >$ ca. 10 kbar $<$ ca. 20 kbar (Fig. 6a).

3.3.1.2. Rb–Sr data. The Rb–Sr data of feldspar, clinozoisite-1, white mica-1, titanite, and whole rock samples scatter, which may reflect (i) initial Sr isotopic heterogeneity of the metamorphic reactants, including the invading fluid, and incomplete mixing and redistribution of Sr (Fig. 6f, Table 3) or (ii) a polystage evolution of some phases. A Rb–Sr isochron, calculated with titanite and white mica, yields 226 ± 4 Ma, which agrees with the $^{206}Pb/^{238}U$ multimineral isochron age. The Rb–Sr system of white mica has been shown to be rather resistant during metamorphic overprint (Mposkos and Wawrzenitz, 1995; Freeman et al., 1997; Glodny et al., 1998). Since white mica and titanite show no compositional zonation (of Fe, Al, Ca, Mg, Si), it is likely that they yield crystallization ages for HT-deformation (Fig. 6a), albeit isotopic equilibrium among the two mineral phases cannot be shown using independent evidence.

The Sr isotopic composition of the low $^{87}Rb/^{86}Sr$ samples feldspar, clinozoisite, and whole rock is more radiogenic than that of titanite. Using these minerals to constrain the Rb–Sr age of white mica would result in a younger age (205 ± 16 Ma). Recrystallization of feldspar and clinozoisite during deformation and exhumation of this rock may have facilitated incorporation of a more radiogenic Sr into these minerals, which would flatten the slope of the isochron and deprive the younger apparent age of geochronological significance (rotated mixing line).

3.3.2. Sample 99144

This sample is a leucocratic granoblastic gneiss from the Orthogneiss Complex (Fig. 1), consisting mainly of K-feldspar, plagioclase, quartz, and minor garnet and epidote. Elongated but internally strain free quartz and feldspar grains show shape preferred orientation and lack of equilibrium grain boundary configurations (Fig. 7b), typically with younger, smaller grains bulging into older, larger ones. Such microfabrics, reflect accumulation of intense strain at high temperatures, especially by dissolution precipitation creep during decompression (Fig. 7a). This type of deformation is typical for most quartzofeldspathic rocks from the Orthogneiss Complex and occurs at low differential stresses and high temperatures (Carter and Tsenn, 1987). Three types of titanite reflect dissolution precipitation creep during the HT deformation. (i) Idiomorphic titanite shows shape preferred orientation parallel to the foliation plane (Fig. 7b) and is interpreted to have precipitated during deformation in presence of fluids. (ii) Titanite occurs as inclusions in feldspar. (iii) Local titanite aggregates display irregular, corroded margins. These are interpreted as remnants of titanite dissolved during deformation. Since this process occurs repeatedly during progressive deformation, all three types of titanite grew essentially coevally. The absence of rutile suggests that syn-deformation *P–T* conditions were below the pressure sensitive titanite-forming reaction Czo + Rut + Q = An + Tit + V.

There are two generations of garnet. The older, brownish garnet together with K-feldspar is characterized by relatively high Mg and Fe contents, irregular grain shape, and corroded margins. The younger, pinkish garnet is smaller and forms hypidiomorphic grains (Fig. 7c). There are also two generations of epidote. Older epidote with an allanite-rich core shows corroded margins and is typically larger than newly formed epidote.

3.3.2.1. U–Pb data. U–Pb analyses were made on clear idiomorphic titanite, clear light-green core-free epidote, and pink second-generation garnet (Table 4). The older brownish garnet was not analysed due to abundant inclusions. All dated mineral phases participated in the dissolution precipitation process, possibly in the presence of fluids. The U–Pb system may have been reset during recrystallization. Provided closed system behaviour, and a homogenous initial Pb isotopic composition, the isochron age is therefore interpreted to constrain deformation controlled by dissolution precipitation creep (at pressures between about 10–20 kbar, below the eclogite stability field) (Fig. 7a). Several fractions of titanite together with epidote and pink garnet yield an U–Pb isochron age of 218 ± 3 Ma (Fig. 7d).

3.4. Localized shear zones associated with emplacement and cooling

Localized shear zones represented by samples 99104, 99105, and 99210 formed at various conditions from medium to low grade and caused emplacement of the UHP subunits in the upper crust. Shear zones represented by samples 99104 and 99105 surround boudins preserving UHP rocks (sample 99101, 99102) within amphibolite facies rocks. A shear zone represented by sample 99210 separates tectonic complexes with differing *PT*-histories (Fig. 1).

3.4.1. UHP eclogite boudin, retrogression and surrounding shear zones (99101–99105, 9837)

To the NW of Changpu, near Yanhe (Orthogneiss Complex) boudins of phengite eclogite and eclogitic

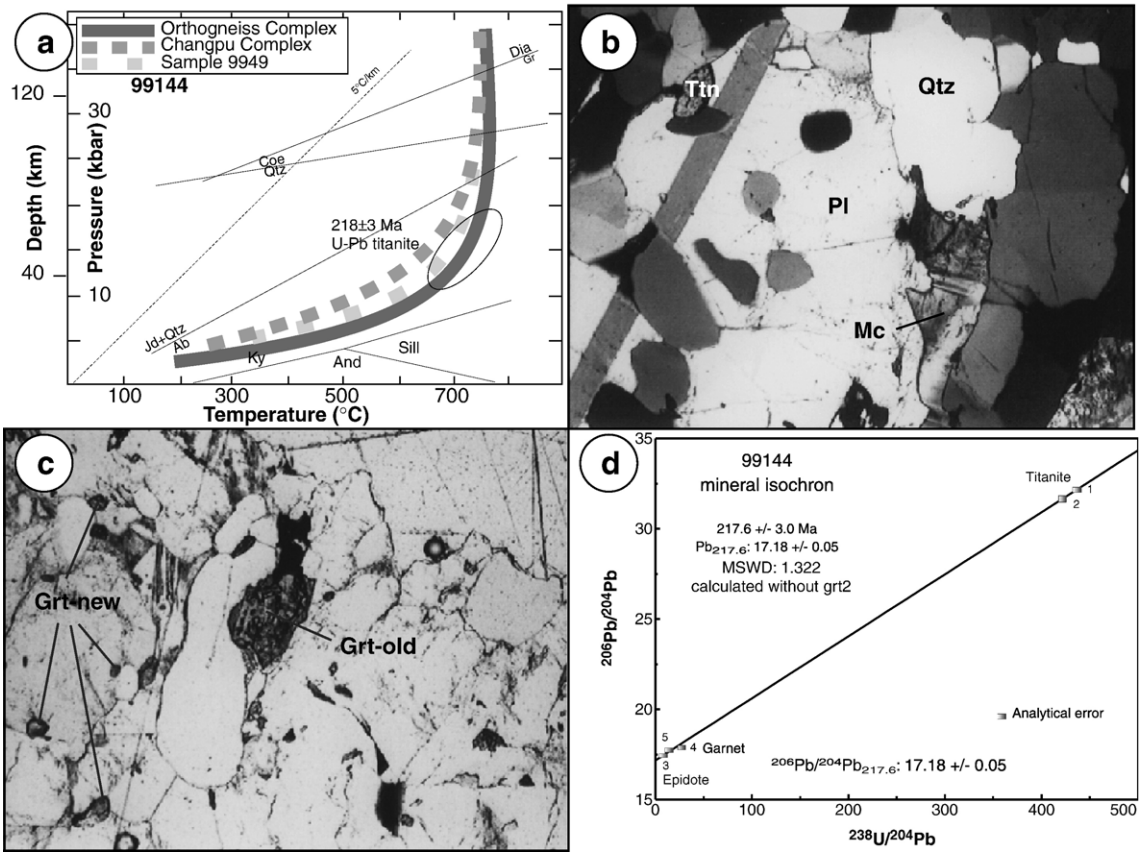

Fig. 7. Leucocratic granoblastic gneiss from Orthogneiss Complex (sample 99144). (a) *PT*-path showing the conditions for syn-deformational titanite growth during a HT deformation episode. Mineral abbreviations according to Kretz (1983). (b) Long axis preferred orientation of idiomorphic syn-deformational titanite (upper left) parallel to the foliation. Plagioclase and quartz show elongate grain shape, defining the foliation plane, and lack equilibrium grain-boundary configurations. Internally strain-free feldspar with lobate grain and phase boundaries suggest strain accumulation by dissolution precipitation creep. Photo is ca. 1.2 mm wide, crossed nicols. (c) Large corroded, old garnet (center of photo) and small idiomorphic, young garnet (upper left, lower left). Young garnet, titanite, and epidote (not shown) crystallized during deformation dominated by dissolution precipitation creep. Photo is ca. 2.3 mm wide, parallel nicols. (d) ^{238}U–^{206}Pb isochron diagram for epidote, garnet, and titanite. The titanite and epidote pair yield an U–Pb isochron age of 218 ± 3 Ma that constrains the high-*T* deformation. Garnet is in Pb-isotopic disequilibrium with titanite and epidote, probably due to inclusions and Pb-inheritance from older garnet.

gneisses occur within leucocratic two-mica gneisses. This assemblage, which is characterized by strong viscosity contrasts, shows locally varying degrees of strain accumulation during exhumation.

The phengite bearing eclogite (sample 99102) shows the UHP mineral assemblage grt+cpx+phg+rt. Preferred orientation of the long axis of cpx crystals (Jd), elongated garnet aggregates, and basal planes of phengite defines a distinct foliation that reflects this UHP deformation event. Using the garnet–omphacite–phengite geobarometer and the garnet–clinopyroxene geothermometer (Powell, 1985; Berman, 1991), peak PT conditions were estimated by Schmid (2001) to 33–35 kbar at 680 °C (Fig. 8a).

The gneissic eclogite shows rare UHP relics of jadeitic clinopyroxene as inclusions in garnet (samples 99101 and 9837) and contains sigma-clasts of former clinopyroxene, which have been replaced by undeformed amphibole–plagioclase symplectites during decompression (Fig. 8b). The clinopyroxene belonged to the UHP assemblage zoisite–(jadeite-rich) clinopyroxene–coesite.

The gneissic eclogite is surrounded by medium grade two-mica gneisses (99103) that were strongly deformed at medium grade. White mica coexisting with biotite formed under medium grade conditions. Exhumation episodes finally resulted in the surrounding biotite gneisses (99104, 99105) in the formation of the mineral assemblage biotite–epidote–oligoclase–quartz

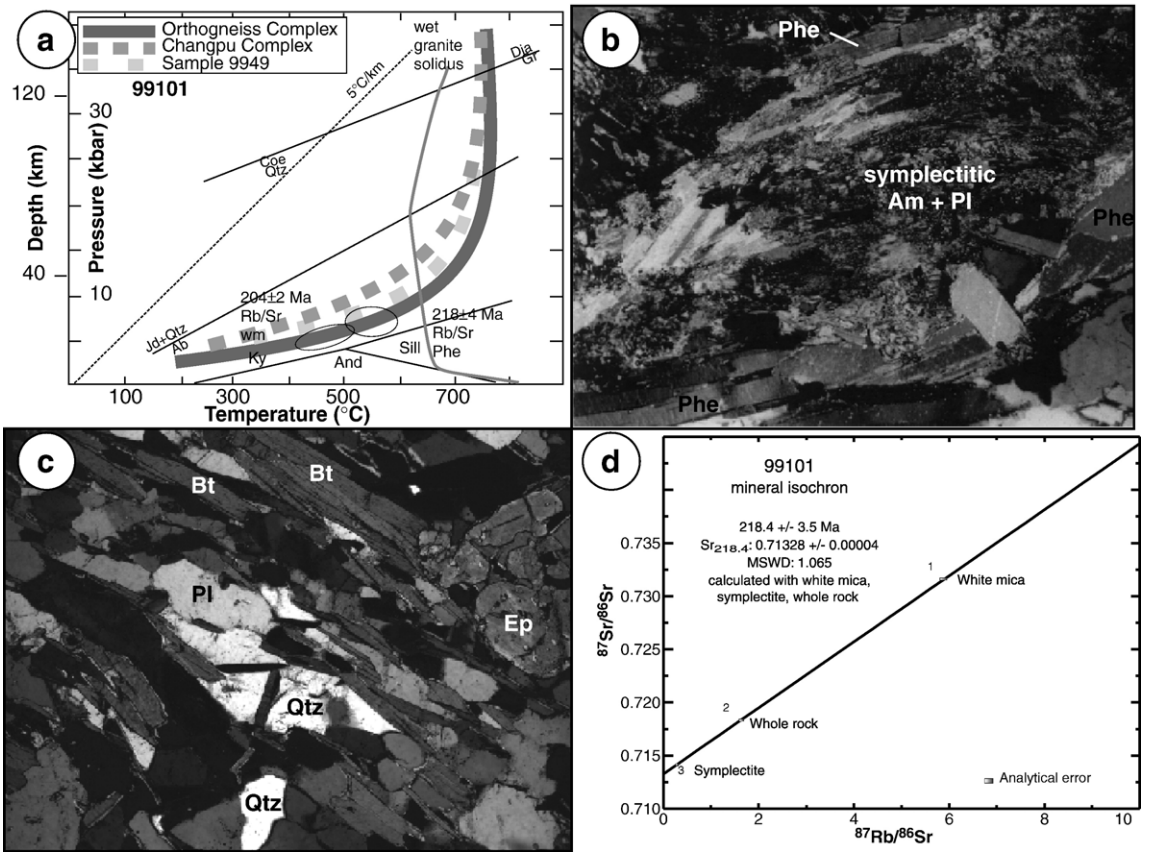

Fig. 8. Samples from retrogressive medium grade shear zones surrounding gneissic eclogites (99101, 99104, 99105). (a) *PT*-path showing the conditions for deformation and mineral growth in retrogressive medium-grade gneisses. Wet granite solidus curve after Stern and Wyllie (1981). Mineral abbreviations according to Kretz (1983). (b) Gneissic eclogite (sample 99101) deformed during medium grade metamorphism. Sigma clast (shear sense top right) consisting of symplectitically intergrown amphibole and plagioclase. Phengitic white mica surround the sigma clast. Photo is ca. 2.3 mm wide, crossed nicols. (c) Typical fabric of gneisses (99104) in shear zone formed during greenschist facies metamorphism. Photo is ca. 2.3 mm wide, crossed nicols. (d) Rb–Sr isochron diagram for minerals from the low-strain domain of the eclogitic gneiss 99101 yielding a white mica age of 218 ± 4 Ma.

(± white mica). The syn-deformational fabric records deformation related with the emplacement of these rocks at a mid-crustal level (Fig. 8c).

3.4.1.1. Rb–Sr data. Access of water during decompression triggered the breakdown of clinopyroxene to amphibole–plagioclase symplectite and the alteration of UHP phengites to less phengitic white mica and biotite (and quartz). Fluids may also have been effective at resetting the Rb–Sr isotopic system. Rb–Sr geochronology using plagioclase–amphibole symplectites, phengitic white mica with a Si content of 3.3 p.f.u., and whole rock from the gneissic eclogite yields an isochron with a slope corresponding to an age of 218 (± 4) Ma (Fig. 8d, Table 3). Provided closed system behaviour and initial isotopic equilibrium among the phases, this age dates the hydration, as well as the exhumation to a depth shallower than required for eclogite formation.

Rare large phengitic white mica grains (Si content 3.4 p.f.u.) from a second sample of the gneissic eclogite (9837) yield a Rb–Sr mineral and whole-rock isochron that defines an age of 236 ± 19 Ma, the large a priori error being due to a low Rb/Sr ratio (Table 3). No UHP mineral relics are preserved in the neighbouring two-mica gneisses (samples 99103 and 99104). Sample 99104 yields a Rb–Sr white mica age of 209 ± 2 Ma (Table 3). This is interpreted as the age of continuing shearing in the gneisses surrounding the more mafic boudins, provided the initial Sr isotopic composition of whole rock used for age calculation did not change after mica recrystallization.

3.4.2. Low grade shear zone bounding the Ganghe Complex

The juxtaposition of the Ganghe unit occurred at even lower metamorphic grade. The Ganghe low-strain domain locally even preserved sedimentary and volcanic structures (Oberhänsli et al., 2002). UHP mineral assemblages are also abundantly preserved. The Ganghe domain is composed of metasedimentary and metavolcanic sequences sandwiched between predominantly orthogenic gneisses. Final juxtaposition of the Ganghe domain against the Orthogneiss Complex along narrow localized shear zones occurred during exhumation at greenschist facies conditions, i.e., relatively late in the overall deformation history. The shear zones are characterized by a distinctly mylonitic fabric with a fine-grained matrix consisting of white mica, quartz, and albite. Up to 3 cm large albite porphyroblasts occur within the matrix. Blastesis was outlasted by shearing. Mylonitization occurred at ca. 500 °C (grt-white mica inclusions in albite), calculated for a reference pressure of 5 kbar.

We analysed the Rb–Sr isotopic composition of feldspar and white mica from a strongly mylonitized albite-white mica gneiss (sample 99210) that formed in such a low-grade mylonite zone (Table 5). This shear zone bounds the Ganghe domain toward the underlying Orthogneiss Complex (east of Changpu; see Schmid (2001) for description) and represents the latest stages in the overall microtextural history. The foliation defined by elongated inclusions in albite is at high angle to the pervasive mylonitic foliation, reflecting non-coaxial strain. The Rb–Sr data yield a Triassic age (204 ± 2 Ma, epidote, albite, and white mica) for medium to low pressure mylonitization, and thus, juxtaposition of the Ganghe domain.

4. Isotopic constraints on the precursors of the UHP rocks

The mafic eclogites, high-grade gneisses, and metacarbonates from the Dabie metamorphic belt have distinct Pb, Nd, and Sr signatures that reflect contrasting sources and precursor histories as well as contrasting mobilization during metamorphism 240 m.y. ago. Variations do occur among the lithologies but are independent from metamorphic grade or relationship with tectonic subunits.

The eclogites and high-grade gneisses are characterized by unradiogenic uranogenic Pb (Fig. 9a), which is typical for derivation from a source that had a retarded Pb evolution due to low $^{238}U/^{204}Pb$ for extended periods of time. The investigated rocks do not show a corresponding retarded evolution in $^{208}Pb/^{204}Pb$ (Fig. 9b), implying that the source $^{232}Th/^{204}Pb$ was not as strongly affected as $^{238}U/^{204}Pb$. The observed Pb isotopic compositions (Tables 2 and 4) fall into the range known from other old high-grade terrains (cf. Taylor et al., 1980; Romer and Bridgwater, 1997; Rudnick and Goldstein, 1990; Zhou et al., 2002) and close to the model evolution-curve for the lower crust (Zartman and Doe, 1981). Thus, the Pb isotopic composition of the eclogites and gneisses suggests the Pb budget of these rocks to be dominated by an old crust precursor that had experienced preferential removal of U during Palaeoproterozoic or Archaean high-grade metamorphism.

Table 5
Rb–Sr data of samples 99210 (low grade shear zone surrounding the Ganghe complex) from the Central Dabie Complex and of the gneiss samples SU291 and SU269 (Pre-Pilot Drill Core PP2, Donghai) from the Sulu UHP complex

Sample no.	Sample	Rb [ppm][a]	Sr [ppm][a]	$^{87}Rb/^{86}Sr$	$^{87}Sr/^{86}Sr$	$\pm 2\sigma_m$
99210.1	White mica	206	32.9	18.2	0.76216	0.00001
99210.2	Whole rock	110	117.7	2.72	0.71632	0.00001
99210.3	Whole rock	104	117.3	2.56	0.71627	0.00001
99210.4	Epidote	23.2	4594	0.01	0.70922	0.00001
99210.6	Quartz–albite	7.0	36.5	0.55	0.71077	0.00001
99210.7	Quartz–albite	4.8	28.4	0.49	0.71083	0.00002
SU291.1	Biotite	497	18.1	81.2	0.94165	0.00002
SU291.2	Biotite	413	42.0	28.7	0.79047	0.00004
SU291.3	White mica	308	36.5	24.6	0.78073	0.00004
SU291.4	White mica	287	28.7	29.1	0.79519	0.00004
SU291.5	Whole rock	36.5	288.2	0.37	0.71026	0.00004
SU291.6	Feldspar	4.1	492.5	0.02	0.70923	0.00001
SU269.1	Biotite	375	2.0	656	2.57743	0.00015
SU269.2	Whole rock	60.8	124.1	1.42	0.71369	0.00001
SU269.3	Plagioclase	21.9	71.6	0.88	0.71283	0.00001
SU269.4	Epidote	0.3	504.9	0.00	0.70952	0.00001

[a] Concentrations were determined by isotope dilution and mixed ^{87}Rb–^{84}Sr tracers.

The gneisses show an even more retarded growth of uranogenic Pb than the eclogites (Fig. 9a). The contrast between the mafic eclogites and high-grade gneisses is not due to contamination of a mantle source by Pb similar to the one in the gneisses. Instead, the slightly more radiogenic Pb in the mafic eclogites may reflect (i) slightly higher $^{238}U/^{204}Pb$ and $^{232}Th/^{204}Pb$ values than in the gneisses, although the values still had to be low in comparison to average mantle or (ii) a younger age for U depletion in the mafic eclogites.

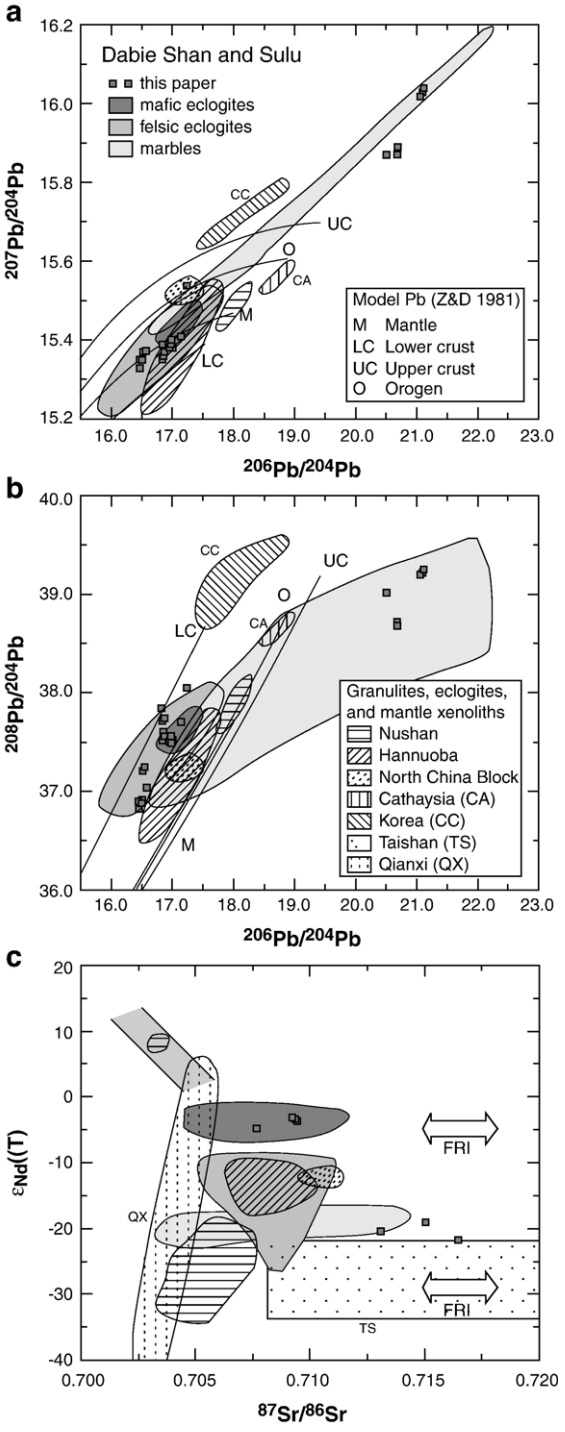

Fig. 9. Initial Pb–Sr–Nd isotopic composition of rock from the Dabie metamorphic belt and geologically and geochemically comparable units of adjacent tectonic blocks. (a) $^{206}Pb/^{204}Pb$–$^{207}Pb/^{204}Pb$ diagram for mafic eclogites, felsic eclogites, and marbles. Reference Pb-growth curves from Zartman and Doe (1981). (b) $^{206}Pb/^{204}Pb$–$^{208}Pb/^{204}Pb$ diagram. (c) $^{87}Sr/^{86}Sr$–ε_{Nd} (T=240 Ma) diagram. FRI=fluid rock interaction. Data sources: (Tables 1, 2, 4, and 6), Chen and Jahn (1998), Ma et al. (2000), Zou et al. (2000), Franz et al. (2001), Cheong et al. (2002), Zhang et al. (2002b), Zheng et al. (2002), Kim et al. (2003), Yu et al. (2003), Huang et al. (2004), Yang et al. (2005), and unpublished data (Romer).

The Pb isotopic composition of carbonate and silicate minerals in marbles from the Central Dabie Complex is radiogenic and falls to the radiogenic end of the Pb trend defined by regional marbles, which had been subducted to UHP conditions. The steep slope of the Pb trend could be obtained by two different processes: (i) Incomplete mixing of Pb from two different sources, one having unradiogenic Pb, the other having relatively radiogenic Pb. (ii) In situ Pb growth in the marbles. The mixing explanation implies a Palaeoproterozoic or older age for the source of the radiogenic end-member, leaving the age of the marble little constrained, whereas the Pb–Pb isochron explanation suggests a Palaeoproterozoic or older age for the marble. Since marble Pb with radiogenic compositions falls to the right of the evolution curve for upper crustal Pb, the source of the radiogenic-mixing end-member or the marble must have been characterized by low Th/U values. The marbles are typically correlated with Neoproterozoic carbonates on the North China Craton (Rumble et al., 2000), yield an ^{238}U–^{206}Pb isochron age of 435 ± 45 Ma (Zheng et al., 1997), may locally be deposited on late Proterozoic granites and gneisses (Schmid, 2001), and experienced Sr mobility during UHP and HP metamorphism as reflected in anomalously unradiogenic Sr isotope signatures (Romer et al., 2003). Therefore, the Pb–Pb array defined by the marbles may reflect mixing rather than in situ Pb evolution.

The Sr–Nd isotope signatures of the mafic eclogites, high-grade gneisses, and marbles show a grouping corresponding to the one obtained for Pb. Most mafic eclogites have ε_{Nd} (T=240 Ma) values around −2 to −6, gneisses range between −9 and −13, and marbles between −16 and −22 (Fig. 9c; Tables 1 and 6). Mafic eclogite and marble samples define subhorizontal trends, which become especially prominent when combined with literature data (Fig. 9c). These trends may reflect

Table 6
Sm–Nd isotope data for whole-rock and mineral samples from the Central Dabie and Sulu Complex, Eastern China

Sample no.	Sample	Sm [ppm][a]	Nd [ppm][a]	$^{147}Sm/^{144}Nd$	$^{143}Nd/^{144}Nd$[b]	$\pm 2\sigma_m$	ε_{Nd}[c]
99210	Quartz–alt	1.29	7.05	0.1107	0.511860	0.000006	−12.5
9834	Clinozoisite	4.42	15.7	0.1701	0.512414	0.000006	−3.6
9834	Clinozoisite	8.72	36.7	0.1437	0.512390	0.000015	−3.2
99210	Whole rock	8.49	45.7	0.1122	0.511897	0.000008	−11.9
99105	Epidote	4.00	2.74	0.8832	0.512601	0.000038	−21.8
99105	Whole rock	1.28	2.83	0.2741	0.511672	0.000008	−21.2
9834	Titanite	223	612	0.2198	0.512436	0.000050	−4.7
9834	Feldspar	0.39	1.74	0.1346	0.512381	0.000010	−3.1
SU291	Biotite	0.17	0.67	0.1514	0.512411	0.000046	−3.0
99104	Epidote	4.21	4.44	0.5727	0.512254	0.000017	−19.0
99105	Whole rock	1.40	3.07	0.2751	0.511713	0.000017	−20.5
SU269	Epidote	11.4	19.5	0.3515	0.512513	0.000016	−7.2

The Rb–Sr isotope systematics of these samples (Tables 2 and 3) are used for dating.
[a] Contents were determined by isotope dilution.
[b] $^{143}Nd/^{144}Nd$ data are normalized with $^{146}Nd/^{144}Nd = 0.7219$.
[c] ε_{Nd} (T) calculated for 240 Ma using λ $^{147}Sm = 6.54E-12$ y^{-1}, $(^{147}Sm/^{144}Nd)^0$ CHUR = 0.1967, and $(^{143}Nd/^{144}Nd)^0$ CHUR = 0.512638.

local decoupling of Sr and Nd due to fluid-transport of Sr. The Sr–Nd systematics of the investigated samples Dabie metamorphic belt generally fall to more radiogenic Sr isotopic compositions than mafic xenoliths and felsic gneisses from Nushan and Qianxi, respectively.

The Pb–Nd–Sr isotopic composition of the high-grade gneisses and mafic eclogites is not readily compared with the isotopic signature of lithologies that may have been related with the precursors of the Dabie UHP rocks. This is mainly due to the incomplete isotopic characterization of other areas for which only Nd and Sr data are available. The Pb isotopic composition, whose budget is likely to be dominated by the crustal source (cf. Dupré and Arndt, 1990; Romer and Bridgwater, 1997), and which possibly is the most sensitive tracer of the provenance of crustal precursor rocks, requires the precursors to have had an Archaean or Palaeoproterozoic lower-crust history, which agrees well with the Archaean and Palaeoproterozoic ages known from U–Pb dating of rocks from the Dabie metamorphic belt (e.g., Hacker et al., 1998, 2000; Maruyama et al., 1998; Ayers et al., 2002).

Compositionally similar rocks that yield Archaean and Palaeoproterozoic zircon ages and have experienced high-grade metamorphism are known from the North China Block, the Yangtze Craton, and Cathaysia. Isotope data from these areas are included in Fig. 9b for comparison with the isotope signature of rocks from the Dabie metamorphic belt. The limited data available suggest that Nushan and Cathaysia possibly did not experience an ancient high-grade event, as their Pb isotope signature does not show high $^{208}Pb/^{204}Pb$ at low $^{206}Pb/^{204}Pb$ values (Fig. 9b), which makes them unlikely precursors. In contrast, several regions in the North China Block show evidence of such an ancient high-grade event. Crustal rocks of similar geochemical signature as the high-grade gneisses in the Dabie metamorphic belt include granulites from Hannuoba, Korea, and possibly the Qianxi high-grade terrain, for which no Pb data are available. Variable contamination of the mantle by ancient lower crust is commonly inferred to explain the isotopic heterogeneity among different high-grade xenoliths in the Hannuoba area (e.g., Zhou et al., 2002; Xu, 2002). The similarity of the isotopic signature of eclogites and high-grade gneisses from the Dabie metamorphic belt with samples from these regions does not constrain the provenance of the subducted protoliths of the Dabie UHP and HP rocks, i.e., derivation from a certain province, but it constrains the kind of crustal evolution the Dabie precursor rocks have had. At the time of Triassic subduction, these precursors of the UHP rocks, showing an ancient lower crustal history, probably had been in an upper crustal position, as is constraint by prograde mineral relics (samples 9864), and pseudomorphs after prograde minerals (sample 99101). This implies that the precursor rocks (carbonates and gneisses) had already undergone multiple reworking prior to Triassic subduction and exhumation. Nevertheless, melts extracted from such reworked high-grade rocks would inherit both the isotopic signature and old zircon.

5. Discussion and conclusion

The integrated geochronological, petrological, and structural study reveals a clear correlation between ages and successive mineral reactions and deformation/recrystallization processes depicted by domainal variations of microfabrics. This correlation precludes

volume diffusion as the major resetting mechanism of the respective isotope systems. Consequently, the age data cannot be interpreted in terms of a thermal/cooling history. The resetting of isotope systems, instead, is associated with (re)crystallisation of titanite, phengitic white mica, and other minerals during changing *P–T* conditions and dissolution precipitation processes related to partial melting and plastic flow involving diffusion creep. This implies that the age data put constraints on the temporal resolution of the *P–T* paths and the kinematic–tectonic histories linked to subduction and exhumation processes of the composite Central Dabie Complex.

5.1. Duration of UHP metamorphism

The 244 ± 3 Ma $^{206}Pb/^{238}U$ age of a pre-mylonitic titanite megacryst from calcsilicate sample 9864 was obtained on pre-maximum-pressure titanite. Petrological evidence and microtextural relationships suggest that this titanite formed during prograde metamorphism. Its U–Pb system remained closed during continuing subduction. The titanite age provides an upper time constraint for the prograde stage of the *P–T* history of this sample and represents a maximum age constraint for UHP metamorphism. It is slightly older than the lower intercept age of zircon (236 ± 32 Ma, Ayers et al., 2002) and Ar–Ar ages of UHP phengite (Hacker et al., 2000) from eclogites interpreted to reflect the age of peak metamorphism. It is in agreement with the U–Pb zircon age of 242 ± 3 Ma for the onset of peak pressure obtained by Li et al. (2004).

Titanite from the pervasively deformed and partially melted quartz–feldspar gneisses (sample 9949) that contains relics of the HP evolution yield a $^{206}Pb/^{238}U$ age of 238 ± 1 Ma. This age corresponds to the exhumation to 18–20 kbar, fluid influx, partial melting, and melt crystallization below the stability field of eclogite and may be associated with a first stage of rapid uplift. If the quartz–feldspar rock and the calcsilicates underwent a common metamorphic *PTt*-evolution, these data imply that these rocks were exposed to UHP metamorphism during a short period from 244 ± 3 to 238 ± 1 Ma.

5.2. High-T deformation and decompressional partial melting

HT-deformation is bracketed between ca. 238 and 218 Ma. Importantly, the $^{206}Pb/^{238}U$ epidote–titanite isochron age of 238 ± 1 Ma of the pervasively deformed quartz–feldspar gneiss (sample 9949) clearly constrains the age of equilibration at high temperatures, including partial melt crystallization below the eclogite (grt+jd) stability field. In this sample, titanite and epidote were stable phases during deformation at ca. 18–20 kbar and titanite formation was associated with dissolution precipitation creep of quartz and feldspar. Melting may have occurred at higher pressures.

The isochron age for amphibolite facies and decompressional partial melting coincides with the age range for UHP metamorphism from other locations (U–Pb zircon and monazite data; Hacker et al., 2000; Ayers et al., 2002) and is older than the age of amphibolite facies overprinting in the Shuanghe jadeite quartzite (dated by $^{208}Pb/^{232}Th$ monazite to 209 ± 4 Ma; Ayers et al., 2002). Obviously, different parts of the Central Dabie Complex followed separate PT-paths, in accordance with new *PT*-data from the Sulu UHP Complex (Zhu et al., 2005). This is corroborated by variations among our and published ages for amphibolite-facies and high-grade deformation.

A U–Pb multi-mineral isochron from the quartzofeldspathic orthogenic gneiss (sample 9834) overlying the Changpu calcsilicate and quartz–feldspar layers (9868 and 9949) yields a $^{206}Pb/^{238}U$ age of 224 ± 2 Ma. This isochron age is defined by mineral phases (clinozoisite, plagioclase, epidote, titanite) that have (re)crystallised during deformation postdating the high-*P* stage. Thus, this age is related to amphibolite facies metamorphism and related deformation microfabrics.

Within quartzofeldspathic gneisses from the Orthogneiss Complex, ages of 218 ± 4 Ma (Rb–Sr white mica age of sample 99101) and 218 ± 3 Ma (U Pb titanite age of sample 99144) are also related to phases (re)crystallized during HT-deformation. Our data demonstrate that from 238 to 218 Ma significant parts of the Central Dabie Complex must have been subjected to partial melting and to several episodes of deformation at medium grade. The age range for HT-deformation at amphibolite facies conditions of samples from different structural positions reflect differential exhumation within the Central Dabie Complex or alternatively imply that the rocks record plastic deformation at high temperatures over a remarkably long period.

5.3. Low-T deformation

During cooling to lower amphibolite and greenschist facies conditions, strain concentrated to widespread pervasive deformation fabrics and localized shear zones with abundant indications for non-coaxial strain, which indicates large differential movement within the Central Dabie Complex. Such shear zones

occur within the Orthogneiss Complex of the Central Dabie Complex and, more importantly, they form bounding structures between orthogneisses and the Ganghe domain. The associated movements involve a significant differential vertical displacement during the decompression and exhumation stage, thus implying contrasting *P–T–t* evolution in various parts of the Central Dabie Complex. The shear zones are associated with the final emplacement of the tectonic subunits and, therefore, the age data constrain the timing of tectonic denudation and juxtaposition of the different subunits in the Central Dabie Complex. Rb–Sr data from syn-deformational white mica of greenschist facies shear zones, the Orthogneiss Complex, as well as bounding mylonites to the Ganghe domain demonstrate that juxtaposition occurred not before ca. 209–204 Ma, which agrees well with the 209 Ma $^{208}Pb/^{232}Th$ monazite age attributed to regional amphibolite facies overprint due to pervasive retrograde fluid infiltration (Ayers et al., 2002).

Rb–Sr ages of syn-deformational white mica are generally significantly older than biotite ages. Syn-deformational white mica and biotite from gneisses from the PP2 drill hole at Donghai, Sulu UHP Complex, yield coinciding Rb–Sr ages of ca. 200 Ma (Table 5), suggesting either more rapid exhumation or late-stage fluid infiltration and recrystallization.

5.4. Differential exhumation of UHP rocks within the Central Dabie Complex

The observed age variation within the composite Central Dabie Complex could express that various samples (i) preserve different stages of the *P–T–t* and deformation history, hence allowing the reconstruction of a large segment of the *P–T–t* and deformation history, or (ii) record different deformation and *P–T–t* histories as a result of differential burial and exhumation histories, providing constraints on translation magnitudes. The close interlayering of former basement and cover rocks implies that detachment and large strain magnitudes must have juxtaposed a variety of source rocks from largely different parts of the lithosphere.

The youngest age interpreted as UHP metamorphism in the eclogite stability field, 226 ± 3 Ma Sm–Nd isochron (Li et al., 2000), is ca. 10 Ma younger than ages for partial melting and HT-amphibolite metamorphism, implying (unless the Sm–Nd isochron represents a rotated mixing line as found in many Variscan high-grade massifs; cf. Romer and Rötzler, 2001) that the Central Dabie Complex did not remain a coherent block during subduction to mantle depth and subsequent exhumation and that some segments were at depths corresponding to the eclogite-stability field while others were subjected to HT-amphibolite facies metamorphism. Thus, UHP metamorphism and exhumation-related HT-deformation may have been polychronous, as described for other high-*P* and UHP terrains, including the Western Alps (Philippot, 1990; Handy and Oberhänsli, 2004), the Erzgebirge (Willner et al., 2000), and the Saxon Granulites (Rötzler and Romer, 2001). The Triassic age of metamorphism and deformation preclude that Cretaceous structures were responsible for the uplift of the Central Dabie Complex to 30 km depth (e.g., Grimmer et al., 2002).

5.5. Deep subduction of (Pre-)Palaeoproterozoic high grade crust: rates of burial and exhumation

The precursor rocks of the Dabie UHP rocks include old crust that had been depleted of U (and K) during Palaeoproterozoic or Archaean high-grade metamorphism. Relatively high density, low heat production, and dryness of these rock may have facilitated deep subduction and limited melting during prograde metamorphism.

Metamorphic peak conditions with maximum pressures of >40 kbar were met at about 240 ± 1 Ma (Hacker et al., 2000). If the prograde 244 ± 3 Ma old titanite megacryst had formed at ca. 20 kbar, the average rate of vertical movement during subduction would be 14 mm/y. If we consider the age of 242 ± 3 Ma for the onset of a peak pressure of 33 kbar (Li et al., 2004), the rate would only slightly deviate (ca. 18 mm/y).

Similarly, if titanite formation at 238 ± 1 Ma occurred at a depth corresponding to 18–20 kbar, initial exhumation to the base of a thickened crust (ca. 60 km) would have proceeded at an average rate of 31 mm/y. This is quite similar to the exhumation rate of UHP rocks of 35 mm/y for the Kokchetav Massif, Kasachstan (Hermann, 2003), about 20 mm/y for the Sulu UHP metamorphic belt (Yoshida et al., 2004), and 34 (and 16) mm/y for Dora Maira (Rubatto and Hermann, 2001), but still lower than the exhumation rates of 100 mm/y that have been reported from the Western Gneiss Region, Norway (Carswell et al., 2003). Subsequent exhumation to the middle crust (10–15 km) occurred at significantly lower rates. Such different rates of exhumation were also documented by Zheng et al. (2003). At ca. 204 Ma, the rocks underwent greenschist facies metamorphism at a depth corresponding to ca. 5 kbar, resulting in an average exhumation rate of 15 mm/y for the period 238 to 204 Ma. However, deformation episodes at 224 and 218 Ma (9834, 99101, 99144)

probably indicate a slowing down of exhumation when rocks reached the lower and middle crust. The lack of precise *P* estimates linked to these ages inhibit resolving changes in the exhumation rates within the 238 to 204 Ma period. This makes the average rate of 15 mm/y a crude estimate.

Rapid exhumation is explained by large density contrasts to the surrounding mantle that give rise to high buoyancy forces, which in combination with the low viscosity of preserved less dense phases triggers detachment of the crustal rocks soon after their deep subduction and result in high rates for early exhumation from the upper mantle to the lower crust (Ernst et al., 1996; Burov et al., 2000; Gerya and Stoeckhert, 2002). A high density contrast between crustal and mantle rocks is not only due to the contrasting chemical composition, but also to the lack of complete transformation of low-density rock-forming minerals (e.g., feldspar) to high-density phases (Oberhänsli et al., 2002; Carswell et al., 2003). Low viscosity in the Central Dabie Complex and the Sulu UHP Complex is implied from textural evidence for partial melting (Wallis et al., 2005) and for diffusion (dissolution precipitation) creep.

Acknowledgments

This study was financially supported by the German Science Foundation DFG (OB 80/20 as a part of the International Continental Deep Drilling Project, SPP 1006 ICDP) and GeoForschungsZentrum Potsdam. We would like to thank Liu Fulai for providing the two samples from the Donghai PP2 drill hole, Sulu UHP Complex. Thanks are extended to P. O'Brian (Potsdam University) for discussions on petrological, and A. Krohe (Münster University) on structural issues, which helped to clarify the manuscript. We thank Rainer Thomas (GFZ Potsdam) for micro-Raman analyses and Dieter Rehde and Oona Appelt (both GFZ Potsdam) for assistance with microprobe analysis. Robert Schmid (Potsdam) and Y.-F. Zheng are thanked for discussions about the Dabie geology. Comprehensive and thorough reviews of J.C. Ayers and an anonymous reviewer are very much appreciated for helping to improve the manuscript and for revealing a number of references we should have included into the first version.

Appendix A. Analytical methods

Mineral concentrates were obtained from microtexturally controlled domains that were cut from thick-sections and thin-slabs. These parts were crushed and minerals were concentrated using standard mineral separation techniques and separation by hand under the binocular. Minerals were dissolved overnight with 52% HF in Teflon vials at 160 °C on a hot plate, dried, and transferred overnight into chloride-form using 6 N HCl at 160 °C on a hot plate.

Sr and Rb were separated using standard cation exchange techniques (Bio Rad AG50 W-X8, 100–200 mesh, 3.8 ml resin volume) in 2.5 N HCl medium. Sr was loaded on single Ta-filaments and its isotopic composition was determined on a VG Sector 54-30 multicollector mass-spectrometer using a triple-jump dynamic-multicollection setup. Rb was loaded on double Ta-filaments and analyzed in static mode. Concentrations were determined with a mixed ^{84}Sr–^{87}Rb tracer. $^{87}Rb/^{86}Sr$ is known better than 1%. $^{87}Sr/^{86}Sr$ data are normalized with $^{86}Sr/^{88}Sr = 0.1194$. Repeated measurement of Sr standard NBS 987 during the measurement period gave 0.710249 ± 0.000004 (2σ reproducibility for $n = 12$ independent analyses). Analytical uncertainties of the individual measurements are reported as $2\sigma_m$. Total procedural blanks are less than 50 pg Sr (Romer et al., 2005).

Nd and Sm were separated using standard cation exchange techniques (HDEHP-coated Teflon, 2 ml resin volume) in 0.18 and 0.4 N HCl medium, respectively. Nd was loaded on double Re-filaments and its isotopic composition was measured on a Finnigan MAT262 multicollector mass-spectrometer using dynamic multicollection. $^{143}Nd/^{144}Nd$ data are normalized with $^{146}Nd/^{144}Nd = 0.7219$. Repeated measurement of La Jolla Nd standard during the measurement period gave $^{143}Nd/^{144}Nd = 0.511850 \pm 0.000004$ (2σ reproducibility for $n = 14$ independent analyses). Concentrations were determined with a mixed ^{149}Sm–^{150}Nd tracer. Analytical uncertainties of the individual measurements are reported as $2s_m$. Total procedural blanks are less than 30 pg Nd (Romer et al., 2005).

U and Pb for minerals and whole-rock samples were separated using standard HBr–HCl ion-exchange chromatography based on the procedure described by Tilton (1973) and Manhès et al. (1978). For whole-rock samples, the procedure was repeated to obtain a better separation from other ions. Pb and U were loaded together on a single Re-filament and analyzed at 1200–1260 and 1350–1400 °C, respectively, on a Finnigan MAT262 multi-collector mass-spectrometer using Faraday collectors for whole-rock samples and Faraday collectors and a secondary-ion multiplier for mineral samples with radiogenic Pb.

Appendix B. Sample locations

Sample	Coordinates[a]	Rock type
9834	N30°47.861/E116°15.223	Clinozoisite–titanite bearing gneiss
9837	N30°46.669/E116°12.490	Gneissic eclogite showing rare UHP relics of jadeitic clinopyroxene as inclusion in garnet
99101	N30°46.669/E116°12.490	Gneissic eclogite showing rare UHP relics of jadeitic clinopyroxene as inclusion in garnet
99102	N30°46.669/E116°12.490	Phengite bearing eclogite
99103	N30°46.669/E116°12.490	Medium grade two-mica gneiss surrounding gneissic eclogite
99104	N30°46.669/E116°12.490	Biotite gneiss
99105	N30°46.669/E116°12.490	Biotite gneiss
9864	N30°42.454/E116°15.007	Titanite bearing calcsilicate
99144	N30°42.243/E116°15.020	Leucocratic granoblastic gneiss from the Orthogneiss Complex
99210	N30°41.782/E116°14.688	Strongly mylonitized albite–white mica gneiss
9949	N30°42.134/E116°23.592	Leucocratic granoblastic white mica–biotite–plagioclase–K-feldspar gneiss

[a] Samples were positioned using a GARMIN 12 GPS system and referenced to WGS 84.

References

Ames, L., Tilton, G.R., Zhou, G., 1993. Timing of collision of the Sino-Korean and Yangtze cratons: U–Pb zircon dating of coesite-bearing eclogites. Geology 21, 339–342.

Ayers, J.C., Dunkle, S., Gao, S., Miller, C., 2002. Constraints on timing of peak and retrograde metamorphism in the Dabie Shan ultrahigh-pressure metamorphic belt, east-central China, using U–Th–Pb dating of zircon and monazite. Chem. Geol. 186, 315–331.

Bard, J.P., 1986. Microtextures of igneous and metamorphic rocks. Petrology and Structural Geology, 2nd ed. D. Reidel Publishing Company, Dordrecht, Holland, p. 264.

Berman, R.G., 1991. Thermobarometry using multiequilibrium calculations: a new technique with petrologic applications. Can. Mineral. 29, 833–855.

Berté, D., Choukroune, P., Gapais, D., 1979. Quartz fabrics and progressive gneissification of granites by simple shear — example of the South Armorican shear zone. Bull. Mineral. 102, 265–272.

Bryant, D.L., Ayers, J.C., Gao, S., Miller, C.F., Zhang, H., 2004. Geochemical, age, and isotopic constraints on the location of the Sino-Korean/Yangtze Suture and evolution of the Northern Dabie Complex, east central China. GSA Bull. 116 (5/6), 698–717.

Burov, E., Jolivet, L., Le Pourhiet, L., Poliakov, A., 2000. A thermomechanical model of exhumation of high pressure (HP) and ultra-high pressure (UHP) metamorphic rocks in Alpine-type collision belts. Tectonophysics 342, 113–136.

Carswell, D.A., Wilson, R.N., Zhai, M.G., 1996. Ultra-high pressure aluminous titanites in carbonate-bearing eclogites at Shuanghe in Dabieshan, central China. Mineral. Mag. 60, 361–471.

Carswell, D.A., Wilson, R.N., Zhai, M.G., 2000. Metamorphic evolution, mineral chemistry and thermobarometry of schists and orthogneisses hosting ultra-high pressure eclogites in the Dabieshan of central China. Lithos 52, 121–155.

Carswell, D.A., Tucker, R.D., O'Brien, P.J., Krogh, T.E., 2003. Coesite micro-inclusions and the U/Pb age of zircons from the Hareidland eclogite in the Western Gneiss Region of Norway. Lithos 67, 181–190.

Carter, N.-L., Tsenn, M.C., 1987. Flow properties of continental lithosphere. Tectonophysics 136, 27–63.

Chavagnac, V., Jahn, B.-M., 1996. Coesite-bearing eclogites from the Bixiling Complex, Dabie Mountains, China; Sm–Nd ages, geochemical characteristics and tectonic implications. Chem. Geol. 133, 29–51.

Chen, J., Jahn, B.-M., 1998. Crustal evolution of southeastern China: Nd and Sr isotopic evidence. Tectonophysics 284, 101–133.

Chen, B., Jahn, B.-M., Wie, C., 2002. Petrogenesis of Mesozoic granitoids in the Dabie UHP complex, central China: trace element and Nd–Sr isotope evidence. Lithos 60, 67–88.

Cheong, C.-S., Kwon, S.-T., Sagong, H., 2002. Geochemical and Sr–Nd–Pb isotopic investigation of Triassic granitoids and basement rocks in the northern Gyeongsang Basin, Korea: implications for the young basement in the East Asian continental margin. Isl. Arc 11, 25–44.

Dupré, B., Arndt, N.T., 1990. Pb isotopic composition of Archean komatiites and sulfides. Chem. Geol. 85, 35–56.

Ernst, W.G., Maruyama, S., Wallis, S.R., 1996. Buoyancy and rapid exhumation of thin slabs of ultrahigh pressure metamorphosed continental crust. Proc. Natl. Acad. Sci. U. S. A. 94, 9532–9537.

Essex, R.M., Gromet, M.P., 2000. U–Pb dating of prograde and retrograde titanite growth during the Scandian orogeny. Geology 28, 419–422.

Faure, M., Lin, W., Shu, L., Sun, Y., Schärer, U., 1999. Tectonics of the Dabieshan (eastern China) and possible exhumation mechanism of ultra high-pressure rocks. Terra Nova 11, 251–258.

Faure, M., Lin, W., Schärer, U., Shu, L., Sun, Y., Arnaud, N., 2003. Continental subduction and exhumation of UHP rocks. Structural and geochronological insights from the Dabieshan (East China). Lithos 70, 213–241.

Franz, L., Romer, R.L., Klemd, R., Schmid, R., Oberhänsli, R., Wagner, T., Dong, Shuwen, 2001. Eclogite-facies quartz veins within metabasites of the Dabie Shan (eastern China): pressure–temperature–time-deformation-path, composition of the fluid phase and fluid flow during exhumation of high-pressure rocks. Contrib. Mineral. Petrol. 141, 322–346.

Freeman, S.R., Inger, S., Butler, R.W.H., Cliff, R.A., 1997. Dating deformation using Rb–Sr in white mica: greenschist facies deformation ages from the Entreloar shear zone, Italian Alps. Tectonics 16, 57–76.

Frost, B.R., Chamberlain, K.R., Schumacher, J.C., 2000. Sphene (titanite): phase relations and role as a geochronometer. Chem. Geol. 172, 131–148.

Fu, B., Touret, J.L.R., Zheng, Y.-F., 2001. Fluid inclusions in coesite-bearing eclogites and jadeite quartzite at Shuanghe, Dabie Shan (China). J. Metamorph. Geol. 19, 531–547.

Gapais, D., Barbarin, B., 1986. Quartz fabric transition in a cooling syn-tectonic granite (Ermitage Massif, France). Tectonophysics 125, 357–370.

Gerya, T.V., Stoeckhert, B., 2002. Exhumation rates of high pressure metamorphic rocks in subduction channels: the effect of rheology. Geophys. Res. Lett. 29, 1024–1028.

Getty, S.R., Gromet, L.P., 1992. Geochronological constraints on ductile deformation, crustal extension and doming about a basement-cover boundary, New England, Appalachians. Am. J. Sci. 292, 359–397.

Glodny, J., Grauert, B., Fiala, J., Veijnar, Z., Krohe, A., 1998. Metapegmatites in the Western Bohemian Massif: ages of crystallization and metamorphic overprint, as constraint by U–Pb zircon, monazite, garnet, columbite and Rb–Sr muscovite data. Geol. Rundsch. 87, 124–134.

Grimmer, J.C., Jonckheere, R., Enkelmann, E., Ratschbacher, L., Hacker, B.R., Blythe, A.E., Wagner, G.A., Wu, Q., Liu, S., Dong, S., 2002. Cretaceous–Cenozoic history of the southern Tan–Lu fault zone: apatite fission track and structural constraints from the Dabie Shan (eastern China). Tectonophysics 359, 225–253.

Hacker, B.R., Ratschbacher, L., Webb, L., Ireland, T., Walker, D., Dong, S.W., 1998. U/Pb zircon ages constrain the architecture of the ultrahigh-pressure Quinling–Dabie orogen, China. Earth Planet. Sci. Lett. 161, 215–230.

Hacker, B.R., Ratschbacher, L., Webb, L.E., McWilliams, M., Calvert, A., Dong, S., Wenk, H.-R., Chateigner, D., 2000. Exhumation of ultrahigh-pressure rocks in east-central China: Late Triassic–Early Jurassic tectonic unroofing. J. Geophys. Res. 105, 13339–13364.

Handy, M., Oberhänsli, R., 2004. Explanatory notes to the map: metamorphic structure of the Alps; age map of the metamorphic structure of the Alps — tectonic interpretation and outstanding problems. Mitt. Österr. Miner. Ges. 149, 201–226.

Heaman, L., Parrish, R., 1991. U–Pb geochronology of accessory minerals. In: Heaman, L., Ludden, J.N. (Eds.), Applications of Radiogenic Isotope Systems to Problems in Geology, Mineral. Assoc. Can., Short Course Hdb., vol. 19, pp. 59–102.

Hermann, J., 2003. Experimental evidence for diamond-facies metamorphism in the Dora-Maira massif. Lithos 70, 163–182.

Holland, T.J.B., Powell, R., 1990. An enlarged and updated internally consistent thermodynamic data set with uncertainties and corrections: the system K_2O–Na_2O–CaO–MgO–MnO–FeO–Fe_2O_3–Al_2O_3–TiO_2–SiO_2–C–H_2–O_2. J. Metamorph. Geol. 8, 89–124.

Huang, X.-L., Xu, Y.-G., Liu, D.-Y., 2004. Geochronology, petrology and geochemistry of the granulite xenoliths from Nushan, East China: implication for a heterogeneous lower crust beneath the Sino-Korean Craton. Geochim. Cosmochim. Acta 68, 127–149.

Jahn, B.-M., 1998. Geochemical and isotopic characteristics of UHP eclogites of the Dabie orogen: implications for continental subduction and collisional tectonics. In: Hacker, B.R., Liou, J.G. (Eds.), When Continents Collide: Geodynamics and Geochemistry of Ultrahigh-Pressure Rocks. Kluwer Acad. Publ., Dordrecht, pp. 203–239.

Jahn, B.-M., Wu, F.Y., Lo, C.H., Tsai, C.H., 1999. Crust–mantle interaction induced by deep subduction of the continental crust: geochemical and Sr–Nd isotopic evidence from post-collisional mafic–ultramafic intrusions of the northern Dabie Complex, central China. Chem. Geol. 157, 119–146.

Kim, Cheong-Bin, Chang, H.-W., Turek, A., 2003. U–Pb zircon ages and Sr–Nd–Pb isotopic compositions for Permian Jurassic plutons in the Ogcheon belt and Ryeongnam massif, Korea: tectonic implications and correlation with the China Quinling Dabie belt and the Japan Hida belt. Isl. Arc 12, 366–382.

Kretz, R., 1983. Symbols for rock-forming minerals. Am. Mineral. 68, 277–279.

Krohe, A., Wawrzenitz, N., 2000. Domainal variations of U–Pb monazite ages and Rb–Sr whole rock-dates in polymetamorphic paragneisses (KTB Drill Core, Germany): influence of strain and deformation mechanisms on isotope systems. J. Metamorph. Geol. 18, 271–291.

Li, S., Jagoutz, E., Chen, Y., Qi, Q., 2000. Sm–Nd and Rb–Sr isotopic chronology and cooling history of ultrahigh pressure rocks and their country rocks at Shuanghe in the Dabie Mountains, central China. Geochim. Cosmochim. Acta 64, 1077–1093.

Li, X.-P., Zheng, Y.-F., Wu, Y.-B., Chen, F.-K., Gong, B., Li, Y.-L., 2004. Low-*T* eclogite in the Dabie terrane of China: petrological and isotopic constraints on fluid activity and radiometric dating. Contrib. Mineral. Petrol. 148, 443–470.

Liou, J.G., Zhang, R.Y., Jahn, B.-M., 1997. Petrology, geochemistry and isotope data on an ultrahigh-pressure jadeite quartzite from Shuanghe, Dabie Mountains, east-central China. Lithos 41, 59–87.

Liu, F.L., Xu, Z.Q., Xue, H.M., 2004a. Tracing the protolith, UHP metamorphism, and exhumation ages of orthogneiss from the SW Sulu terrane (eastern China): SHRIMP U–Pb dating of mineral inclusion-bearing zircons. Lithos 78, 411–429.

Liu, F.L., Xu, Z.Q., Liou, J.G., Song, B., 2004b. SHRIMP U–Pb ages of ultrahigh-pressure and retrograde metamorphism of gneisses, south-western Sulu terrane, eastern China. J. Metamorph. Geol. 22, 315–326.

Ma, C., Ehlers, C., Xu, C., Li, Z., Yang, K., 2000. The roots of the Dabieshan ultrahigh-pressure metamorphic terrane: constraints from geochemistry and Nd–Sr isotope systematics. Precambrian Res. 102, 279–301.

Mancktelow, N.S., Pennacchioni, G., 2004. The influence of grain boundary fluids on the microstructure of quartz–feldspar mylonites. J. Struct. Geol. 26, 47–69.

Manhès, G., Minster, J.F., Allègre, C.J., 1978. Comparative uranium–thorium–lead and rubidium–strontium study of the Saint Séverin amphoterite: consequences for early solar system chronology. Earth Planet. Sci. Lett. 39, 14–24.

Maruyama, S., Tabata, H., Nutman, A.P., Morikawa, T., Liou, J.G., 1998. SHRIMP U–Pb geochronology of ultrahigh-pressure metamorphic rocks of the Dabie Mountains, central China. Cont. Dyn. 3, 72–85.

Massonne, H.-J., Szpurka, Z., 1997. Thermodynamic properties of white micas on the basis of high-pressure experiments in the systems K_2O–MgO–$A1_2O_3$–SiO_2–H_2O and K_2O–FeO–$A1_2O_3$–SiO_2–H_2O. Lithos 4, 229–250.

Mattauer, M., Matte, P., Malavielle, J., Tapponnier, P., Maluski, H., Xu, Z.Q., Lu, Y.L., Tang, Y.Q., 1985. Tectonics of the Quinling Belt — buildup and evolution of eastern Asia. Nature 317, 496–500.

Mposkos, E., Wawrzenitz, N., 1995. Metapegmatites and pegmatites bracketing the time of HP-metamorphism in polymetamorphic rocks of the E-Rhodope, N-Greece. Proc. XV Congr. Carpatho-Balcan Geol. Assoc., Sept. 95, Athens, Geol. Soc. Greece, Spec. Publ., vol. 4, pp. 602–608.

Oberhänsli, R., Martinotti, G., Schmid, R., Liu, X., 2002. Preservation of primary volcanic textures in the ultrahigh-pressure terrain of Dabie Shan. Geology 30, 699–702.

Okay, A.I., 1993. Petrology of a diamond and coesite-bearing metamorphic terrain: Dabie Shan, China. Eur. J. Mineral. 5, 659–673.

Okay, A.I., Xu, S., Sengör, A.M.C., 1989. Coesite from the Dabie Shan eclogites, central China. Eur. J. Mineral. 1, 595–598.

Passchier, C.W., Trouw, R.A.J., 1996. Microtectonics. Springer Verlag, p. 325.
Philippot, P., 1990. Opposite vergence of nappes and crustal extension in the French–Italian Western Alps. Tectonics 9, 1143–1164.
Powell, R., 1985. Regression diagnostics and robust regression in geothermometer/geobarometer calibration: the garnet–clinopyroxene geothermometer revisited. J. Metamorph. Geol. 3, 327–342.
Ratschbacher, L., Hacker, B.R., Webb, L.E., McWilliams, M., Ireland, T., Dong, S., Calvert, A., Chateigner, D., Wenk, H.R., 2000. Exhumation of the ultrahigh-pressure continental crust in east central China: Cretaceous and Cenozoic unroofing and the Tan–Lu fault. J. Geophys. Res.-Solid Earth 105, 13303–13338.
Romer, R.L., 2001. Lead incorporation during crystal growth and the misinterpretation of geochronological data from low-$^{238}U/^{204}Pb$ metamorphic minerals. Terra Nova 13, 258–263.
Romer, R.L., Bridgwater, D., 1997. Geochronologic significance of lead lines from old cratons. Chem. Geol. 136, 125–133.
Romer, R.L., Rötzler, J., 2001. *P–T–t* evolution of ultrahigh-temperature granulites from the Saxon Granulite Massif, Germany: Part II. Geochronology. J. Petrol. 41, 2015–2032.
Romer, R.L., Rötzler, J., 2003. Effect of metamorphic reaction history on the U–Pb dating of titanite. In: Vance, D., Müller, A., Villa, I. (Eds.), Geochronology: Linking the Isotopic Record with Petrology and Textures, Geol. Soc. London, Spec. Publ., vol. 220, pp. 147–158.
Romer, R.L., Xiao, Y., 2005. Initial Pb–Sr(–Nd) isotopic heterogeneity in a single allanite–epidote crystal: implications of reaction history for the dating of minerals with low parent-to-daughter ratios. Contrib. Mineral. Petrol. 148, 662–674.
Romer, R.L., Wawrzenitz, N., Oberhänsli, R., 2003. Anomalous unradiogenic $^{87}Sr/^{86}Sr$ ratios in ultrahigh-pressure crustal carbonates — evidence for fluid infiltration during deep subduction? Terra Nova 15, 330–336.
Romer, R.L., Heinrich, W., Schröder-Smeibidl, B., Meixner, A., Fischer, C.-O., Schulz, C., 2005. Elemental dispersion and stable isotope fractionation during reactive fluid-flow and fluid immiscibility in the Bufa del Diente aureole, NE-Mexico: evidence from radiographies and Li, B, Sr, Nd, and Pb isotope systematics. Contrib. Mineral. Petrol. 149, 400–429.
Rötzler, J., Romer, R.L., 2001. *P–T–t* evolution of ultrahigh-temperature granulites from the Saxon Granulite Massif, Germany: Part I. Petrology. J. Petrol. 41, 1995–2013.
Rowley, D.B., Xue, F., Tucker, R.D., Peng, Z.X., Baker, J., Davis, A., 1997. Ages of ultrahigh pressure metamorphism and protolith orthogneisses from the eastern Dabie Shan: U/Pb zircon geochronology. Earth Planet. Sci. Lett. 151, 191–203.
Rubatto, D., Hermann, J., 2001. Exhumation as fast as subduction? Geology 29, 3–6.
Rudnick, R.L., Goldstein, S.L., 1990. The Pb isotopic compositions of lower crustal xenoliths and the evolution of lower crustal Pb. Earth Planet. Sci. Lett. 98, 192–207.
Rumble, D., Wang, Q., Zhang, R., 2000. Stable isotope geochemistry of marbles from the coesite UHP terrains of Dabieshan and Sulu, China. Lithos 52, 79–95.
Schmid, R., 2001. Geology of ultra-high-pressure rocks from the Dabie Shan, eastern China. Diss. Inst. Geowiss. Universität Potsdam, p. 141.
Schmid, R., Franz, L., Oberhänsli, R., Dong, S., 2000. High Si-phengite, mineral chemistry and *P–T* evolution of ultra-high-pressure eclogites and calc-silicates from the Dabie Shan, eastern PR China. Geol. J. 34, 185–207.
Schmid, R., Romer, R.L, Franz, L., Oberhänsli, R., Martinotti, G., 2003. Basement-cover sequences within the UHP unit of the Dabie Shan. J. Metamorph. Geol. 21, 531–538.
Steiger, R.H., Jäger, E., 1977. Subcommission of geochronology: convention on the use of decay constants in geo- and cosmochronology. Earth Planet. Sci. Lett. 36, 359–362.
Stern, C.R., Wyllie, P.J., 1981. Phase relationships of I-type granite with H_2O to 35 kilobars: the Dinkey Lajes biotite–granite from the Sierra Nevada batholith. J. Geophys. Res. 86, 412–420.
Taylor, P.N., Moorbath, S., Goodwin, R., Petrykowski, A., 1980. Crustal contamination as an indicator of the extent of early Archaean continental crust: Pb isotopic evidence from the late Archaean gneisses of West Greenland. Geochim. Cosmochim. Acta 44, 1437–1453.
Tilton, G.R., 1973. Isotopic lead ages of chondritic meteorites. Earth Planet. Sci. Lett. 19, 321–329.
Tsai, C.H., Liou, J.G., 2000. Eclogite-facies rocks and inferred ultrahigh-pressure metamorphism in the North Dabie Complex, central China. Am. Mineral. 85, 1–8.
Vernon, R.H., 1999. Quartz and feldspar microstructures in metamorphic rocks. Can. Mineral. 37, 513–524.
Wallis, S., Tsuboi, M., Suzuki, K., Fanning, M., Jiang, L., Tanaka, T., 2005. Role of partial melting in the evolution of the Sulu (eastern China) ultrahigh-pressure terrane. Geology 33, 129–132.
Wang, X., Liou, J.G., 1991. Regional ultrahigh-pressure coesite-bearing eclogitic terrane in central China: evidence from country rocks, gneiss, marble, and metapelite. Geology 19, 933–936.
Wang, X., Neubauer, F., Genser, J., Yang, W., 1998. The Dabie UHP unit, central China: a Cretaceous extensional allochthon superposed on a Triassic orogen. Terra Nova 10, 260–267.
Wawrzenitz, N., Krohe, A., 1998. Exhumation and doming of the Thasos Metamorphic Core Complex (S'Rhodope, Greece): structural and geochronological constraints. Tectonophysics 285, 301–332.
Webb, L., Hacker, B.R., Ratschbacher, L., McWilliams, M.O., Dong, S.W., 1999. Thermochronologic constraints on deformation and cooling history of high- and ultrahigh-pressure rocks in the Quinling–Dabie orogen, eastern China. Tectonics 18, 621–638.
Willner, A.P., Krohe, A., Maresch, W.V., 2000. Interrelated *PTt*d-paths in the Variscan Erzgebirge Dome (Saxony, Germany): constraints on the rapid exhumation of high-pressure rocks from the root zone of a collisional orogen. Int. Geol. Rev. 42, 64–85.
Xiao, Y., Hoefs, J., van den Kerkhof, A.M., Fiebig, J., Zheng, Y., 2000. Fluid history of UHP metamorphism in Dabie Shan, China: a fluid inclusion and oxygen isotope study on the coesite-bearing eclogite from Bixiling. Contrib. Mineral. Petrol. 139, 1–16.
Xie, Z., Zheng, Y.-F., Jahn, B.-M., Ballèvre, M., Chen, J., Gautier, P., Gao, T., Gong, B., Zhou, J., 2004. Sm–Nd and Rb–Sr dating of pyroxene–garnetite from North Dabie in east-central China: problem of disequilibrium due to retrograde metamorphism. Chem. Geol. 206, 137–158.
Xu, Y.G., 2002. Evidence for crustal components in the mantle and constraints on crustal recycling mechanisms: pyroxenite xenoliths from Hannuoba, North China. Chem. Geol. 182, 301–322.
Xu, S., Okay, A.I., Sengör, A.M.C., Su, W., Liu, Y., Jiang, L., 1992. Diamond from Dabie Shan metamorphic rocks and its implication for tectonic setting. Science 256, 80–82.
Xu, S., Liu, Y., Chen, G., Roberto, C., France, R., He, M., Liu, H., 2003. New finding of micro-diamonds in eclogites from Dabie–Sulu region in central-eastern China. Chin. Sci. Bull. 48, 988–994.

Xue, F., Rowley, D.B., Tucker, R.D., Peng, Z.X., 1997. U–Pb zircon ages of granitoid rocks in the North Dabie Complex, eastern Dabie Shan. J. Geol. 105, 744–753.

Yang, J.-H., Chung, S.-L., Wilde, S.A., Wu, F.-Y., Chu, M.-F., Lo, C.-H., Fan, H.-R., 2005. Petrogenesis of post-orogenic syenites in the Sulu Orogenic Belt, East China: geochronological, geochemical and Nd–Sr isotopic evidence. Chem. Geol. 214, 99–125.

Ye, K., Liu, J.-B., Cong, B.-L., Ye, D.-N., Xu, P., Omori, S., Maruyama, S., 2002. Ultrahigh-pressure (UHP) low-Al titanites from carbonate-bearing rocks in Dabieshan–Sulu UHP terrain (eastern China). Am. Mineral. 87, 875–881.

Yoshida, D., Hirajima, T., Ishiwatari, A., 2004. Pressure–temperature path recorded in the Yangkou garnet peridotite, in Su-Lu ultrahigh-pressure metamorphic belt, eastern China. J. Petrol. 45, 1125–1145.

Yu, J.-H., Xu, X., O'Reilly, S., Griffin, W.L., Zhang, M., 2003. Granulite xenoliths from Cenozoic basalts in SE China provide geochemical fingerprints to distinguish lower crust terranes from the North and South China tectonic blocks. Lithos 67, 77–102.

Zartman, R.E., Doe, B.R., 1981. Plumbotectonics — the model. Tectonophysics 75, 135–162.

Zhang, H., Gao, S., Zhong, Z., Zhang, B., Zhang, L., Hu, S., 2002a. Geochemical and Sr–Nd–Pb isotopic compositions of Cretaceous granitoids: constraints on tectonic framework and crustal structure of the Dabieshan ultrahigh-pressure metamorphic belt. China. Chem. Geol. 186, 281–299.

Zhang, H.-F., Sun, M., Zhou, X.-H., Fan, W.-M., Zhai, M.-G., Yin, J.-F., 2002b. Mesozoic lithosphere destruction beneath the North China Craton: evidence from major-, trace-element and Sr–Nd–Pb isotope studies of Fangcheng basalts. Contrib. Mineral. Petrol. 144, 241–253.

Zhao, Z.-F., Zheng, Y.-F., Wei, C.-S., Wu, Y.-B., Chen, F.-K., Jahn, B.-M., 2005. Zircon U–Pb age, element and C–O isotope geochemistry of post-collisional mafic–ultramafic rocks from the Dabie orogen in east-central China. Lithos 83, 1–28.

Zheng, Y.-F., Fu, B., Gong, B., Xiao, Y., Ge, N., 1997. U–Pb dating of marble associated with eclogite from the Dabie Mountains, East China. Chin. J. Geochem. 16, 193–201.

Zheng, Y.-F., Fu, B., Li, Y.-L., Xiao, Y.-L., Li, S.-G., 1998. Oxygen and hydrogen isotope geochemistry of ultrahigh pressure eclogites from the Dabie Mountains and the Sulu terrane. Earth Planet. Sci. Lett. 155, 113–129.

Zheng, Y.-F., Wang, Z.-R., Li, S.-G., Zhao, Z.-F., 2002. Oxygen isotope equilibrium between eclogite minerals and its constraints on mineral Sm–Nd chronometer. Geochim. Cosmochim. Acta 66, 625–634.

Zheng, Y.-F., Fu, B., Gong, B., Li, L., 2003. Stable isotope geochemistry of ultrahigh pressure metamorphic rocks from the Dabie–Sulu orogen in China: implications for geodynamics and fluid regime. Earth Sci. Rev. 62, 105–161.

Zheng, Y.-F., Zhou, J.-B., Wu, Y.-B., Xie, Z., 2005. Low-grade metamorphic rocks in the Dabie–Sulu orogenic belt: a passive-margin accretionary wedge deformed during continent subduction. Int. Geol. Rev. 47, 851–871.

Zhou, X., Sun, M., Zhang, G., Chen, S., 2002. Continental crust and lithospheric mantle interaction beneath North China: isotopic evidence from granulite xenoliths in Hannuoba, Sino-Korean craton. Lithos 62, 111–124.

Zhu, Y.-F., Massonne, H.-J., Theye, T., Xu, Z.-Q., 2005. Eclogites from the CCSD — different *PT* paths as indication for a subduction channel environment. Mitt. Österr. Mineral. Ges. 150, 178.

Zou, H., Zindler, A., Xu, X., Qi, Q., 2000. Major, trace element, and Nd, Sr and Pb isotope studies of Cenozoic basalts in SE China: mantle sources, regional variations, and tectonic significance. Chem. Geol. 171, 33–47.